Time Correlation Study in DEAP-3600 Dataset

by

Danial Papi

A thesis submitted in partial fulfillment of the requirements for the degree of

Master of Science

Department of Physics

University of Alberta

Abstract

DEAP-3600 is a single-phase dark matter experiment that utilizes 3.3 tonnes of liquid argon as a scintillation target to detect Weakly Interacting Massive Particles (WIMPs). Two significant challenges in the DEAP-3600 experiment are alpha particles produced in the acrylic vessel neck and dust, which can mimic a WIMP signal. In this thesis, the ^{214}Bi-^{214}Po decay chain was identified in the three-year dataset based on the time correlation. The study demonstrated that degraded alphas originated in dust. A comparison of the time distribution from dust and TPB-coated surface alpha particles showed differences, demonstrating that most dust is not TPB-coated. Time correlation allows us to identify the ^{220}Rn-^{216}Po decay chain. Comparing surface alphas from ^{214}Bi-^{214}Po and ^{220}Rn-^{216}Po revealed differences in their energy distribution, indicating that the alphas from ^{220}Rn-^{216}Po may have originated in the acrylic. A toy Monte Carlo simulation was used to investigate the differences observed in the alpha energy distributions. Although this model could account for some characteristics of the energy distribution, it could not fully explain it.

Contents

List of Tables

List of Figures

Glossary

A | C | D | E | G | L | M | N | P | R | S | T | W

A

AP AfterPulsing.

AV Acrylic Vessel.

C

CMB Cosmic Microwave Background.

D

DAQ Data AcQuisition.

DEAP Dark matter Experiment using Argon Pulse-shape Discrimination.

E

EM ElectroMagnetic.

ER Electron Recoil.

G

GAr Gaseous Argon.

L

LAr Liquid Argon.

M

MBL MBLikelihood postion fitter (Page 36).

MC Monte Carlo.

N

NR Nuclear Recoil.

P

PE PhotoElectron.

PMT PhotoMultiplier Tube.

PSD pulse shape discrimination.

R

ROI Region of Interest.

S

SNO Sudbury Neutrino Observatory.

T

TF2 TimeFit2.

TPB TetraPhenyl Butadiene.

W

WIMP Weakly Interacting Massive Particle.

Chapter 1

Introduction

1.1 Evidence for Dark Matter

For a long time, most of the research in physics and astrophysics has relied on visual observations to map the cosmos. However, these observations are contingent on electromagnetic interactions. There is strong evidence that 85% of all matter in the Universe is invisible, referred to as dark matter [1]. While dark matter can't be seen directly, its presence is indicated by its gravitational effect on ordinary visible matter, giving significant evidence that large amounts of dark matter exist. Measurements conducted by the Planck collaboration suggest that only 4.8% of the Universe's energy density is constituted of ordinary matter. The necessity for dark matter is established by a substantial collection of data from the past 100 years, which reveals a mass deficiency on galactic and cosmological scales. Alternative hypotheses, such as modified theories of gravity, have difficulties explaining the observations [2, 3].

In 1933, Fritz Zwicky, a Swiss astrophysicist, first proposed the concept of dark matter when he studied the Coma Cluster. He applied the virial theorem of classical mechanics, which relates the average kinetic energy (KE_{ave}) of a system to its average gravitational potential energy (GPE_{ave}), using the equation $KE_{ave} = -\frac{1}{2}GPE_{ave}$. By observing the shift in spectral lines, Zwicky determined that the velocities of galaxies relative to the cluster's average were much higher than expected based on the average value calculated using individual galaxies as test particles in the virial theorem. This discrepancy led him to suggest the presence of dark matter in quantities much greater than luminous matter, thus coining the term "dark matter." Although this observation initiated the idea of the missing matter, it did not gain much attention until the 1970s due to the incorrect value of the Hubble constant used in Zwicky's calculations [4, 5, 6].

In 1970, Kenneth Charles Freeman, the Australian astronomer, conducted research [7] that was followed by Vera Rubin, Kent Ford, who provided further proof of the presence of dark matter through the examination of galaxy rotation curves [8]. Newton's law of gravitation states that the circular velocity of an orbit of radius, r, is given by $v(r) = \sqrt{\frac{GM(r)}{r}}$, where $M(r)$ is the mass inside the orbit [9]. However, when the orbital radius lies in the outer region of the visible disk of the galaxy, the observed rotation curves, such as the one shown in Figure 1.1, display a flat behavior that is not in accordance with the predictions made by the law of gravitation. This discrepancy was found for many galaxies, and Rubin and Ford concluded that there must be a significant amount of dark matter in the outskirts of the galaxies to compensate and allow the outer regions to rotate at a similar velocity to central regions. The flat rotation curve in Figure 1.1 can be accurately modeled by the inclusion of a spherical dark halo with $\rho \propto 1/r^2$, where ρ represents the density of the dark matter. This halo is composed of non-luminous matter.

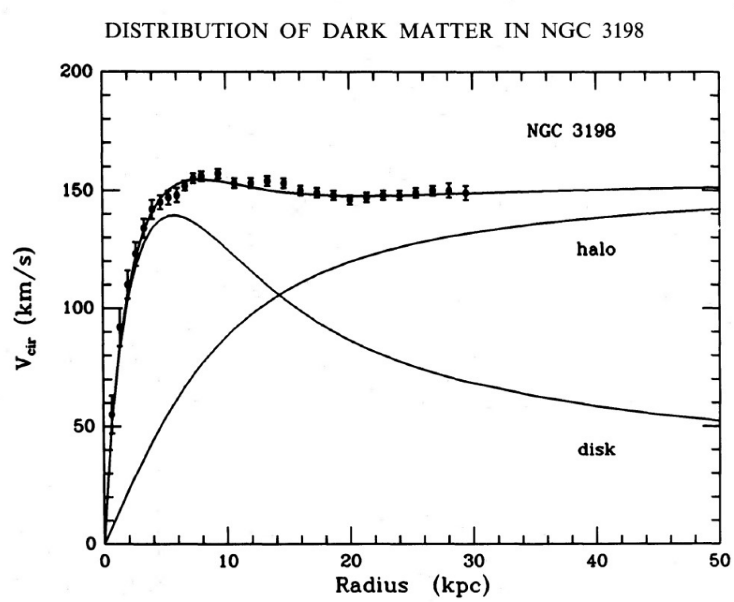

Figure 1.1: The rotation curve of NGC3198 is depicted in this figure, with two components: a visible component (disk) and a dark halo component (halo) [10].

Another evidence of dark matter comes from gravitational lensing, a phenomenon in which the gravitational field of a large mass bends the trajectory of light. This provides an observable effect that indicates the presence of dark matter on a galactic scale. According to general relativity, massive objects cause spacetime to curve, and this curved geometry acts as a lens, changing the path of light emitted by distant sources. By measuring the amount of distortion, observers on Earth can estimate the masses of the gravitational lenses. The equation for the angle of refraction is [11]:

$$\Phi_{GL} = \frac{4GM}{c^2 r}, \tag{1.1}$$

where G is the constant of gravity, M is the mass of the object, r is the minimal distance between the object and light ray, and c is the light speed. This method provides a way of estimating the masses of objects without making assumptions about the nature of the mass, whether it be ordinary or dark matter.

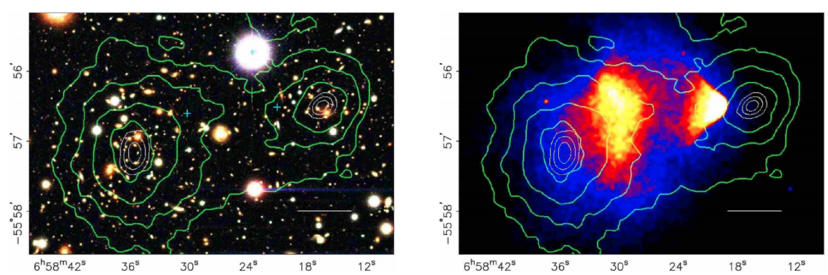

Figure 1.2: The Bullet cluster (1E 0657) is a merger of two clusters of galaxies and is depicted in two images: the left panel shows an image taken by the Magellan IMACs Telescope, and the right panel shows an artificially coloured image from the Chandra X-ray. The green contours in both panels show the mass distribution reconstructed from weak gravitational lensing, and the colour at the right shows the X-ray emission, produced by bremsstrahlung emission from hot ionized gas [12].

The 2006 observation of the Bullet cluster, a collision of two galaxy clusters 3.7 billion light years away, provided additional evidence for dark matter and made explanation from modified gravity difficult as it would require mass to be concentrated in the same region as the visible matter. The hot gas of the two galaxies, observed in the X-ray, makes up most of the baryonic matter, which, during the collision, interacts via electromagnetic forces and is slowed down much more than the stars. Gravitational lensing studies of the merger revealed the centre of mass was spatially displaced from the hot gas, suggesting that large amounts of dark matter exist in both galaxy clusters that did not interact with the gas during the collision. Clowe et al. [12] measured the lensing from this cluster, displayed in Figure 1.2, and found that the mass distribution measured by gravitational lensing matched the locations of the galaxies, not the hot gas observed by Chandra. However, the mass of the hot gas is much larger than that of the galaxies. This discrepancy suggests the presence of additional hidden mass, which does not interact strongly with itself or with the gas, allowing it to pass through the collision without significant interactions, similar to the behaviour of stars and galaxies. This observation provides strong evidence for the existence of dark matter [3].

The most accurate estimation of the Universe's total amount of dark matter is derived from measurements of the Cosmic Microwave Background (CMB). The CMB radiation originated during the Big Bang and separated from matter around 380,000 years after that event. This separation occurred when the Universe cooled sufficiently, allowing basic neutral hydrogen atoms to form. Photons remaining from this period have been traveling across space, losing energy as their wavelengths stretch due to the universe expanding. Presently, these photons have cooled to around 2.73 Kelvin. Penzias and Wilson first measured CMB photons [13].

Observations of the CMB align closely with the minimal ΛCDM (Lambda-Cold Dark Matter) cosmological model, which outlines the pace of expansion in a flat Universe (with no curvature). This model accounts for four components: regular matter, dark matter, radiation (like photons and relativistic neutrinos), and dark energy. The basic ΛCDM model relies on different cosmological factors, and their specific values are found by fitting the power spectrum with the model's prediction. These factors involve H_0, representing the Hubble constant—a measure of how fast the Universe expands. Also, there are Ω_i for each of the four components. The density parameter Ω_i for each element refers to the ratio of its density to the critical density $\rho_{critical}$, which is the current value necessary for a spatially flat Universe. The total density has been measured to be incredibly close to this critical density. The densities for baryonic matter, dark matter, radiation, and dark energy are indicated respectively as Ω_b, Ω_c, Ω_{rad}, and Ω_Λ.

The temperature anisotropies observed in the CMB can be expressed as an expansion in terms of spherical harmonics $Y_{\ell m}(\theta, \phi)$ [14]:

$$\frac{\delta T}{T}(\theta, \phi) = \sum_{l=2}^{+\infty} \sum_{m=-l}^{+l} a_{lm} Y_{lm}(\theta, \phi), \tag{1.2}$$

where a_{lm} are the expansion coefficients. The variance C_l of the expansion coefficients is defined as:

$$C_l = \frac{1}{2l+1} \sum_{m=-l}^{l} |a_{lm}|^2 \tag{1.3}$$

$l(l+1)C_l/2\pi$ is plotted as a function of the multipole moment l in Figure 1.3. This figure illustrates how the power spectrum aligns with the ΛCDM model, as outlined in the 2018 Planck report [15]. These recent findings pinpoint the density contributions: $\Omega_b h^2 = 0.022383$ for baryonic matter and $\Omega_c h^2 = 0.12011$ for dark matter [15]. Here, $h = H_0/(100 \text{ km/s/Mpc})$, with $H_0 = 37.4$ km/s/Mpc is the Hubble constant.

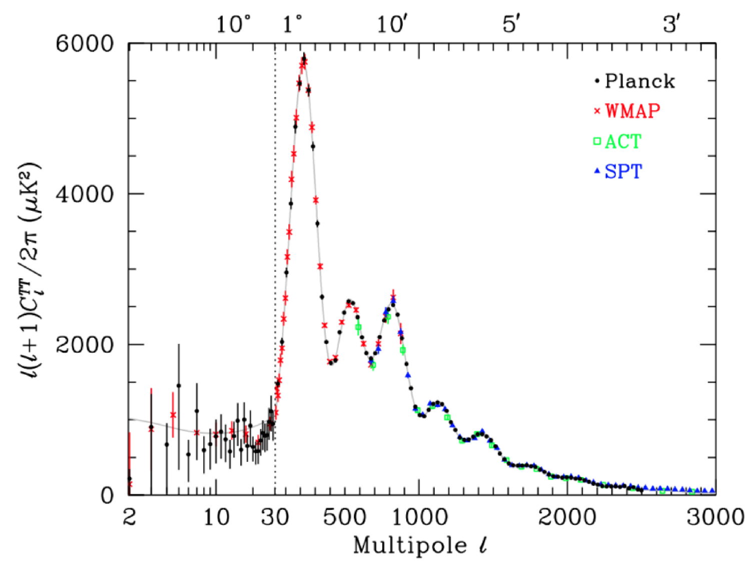

Figure 1.3: This figure shows the CMB temperature anisotropies plotted against the multipole moment l. The lower x-axis is logarithmic for $l < 30$, transitioning to linear for higher values. The data points correspond to measurements from the experiments listed in the legend. The curve represents Planck's best-fit model based on the ΛCDM [1].

1.2 Dark Matter Candidates

From the evidence discussed earlier, it's clear that dark matter exists in the Universe, although its exact nature remains a mystery. We have several possible candidates for what it might be. Theoretical studies suggest that the early Universe couldn't have produced enough baryonic matter to match the mass needed for dark matter [16]. This indicates that a significant portion of the universe, and in particular dark matter, most likely consists of non-baryonic matter.

In searching for dark matter, scientists categorize candidates as hot, cold, or warm based on their relativistic nature in the early universe. Hot dark matter, with a mass around tens of eV, is too relativistic to explain how galaxies and clusters formed and, as a result, can contribute only a tiny portion to the overall amount of dark matter.

In the search for dark matter within particle physics, the candidates are limited to massive (from GeV to TeV), weakly interacting particles that aren't part of the Standard Model. This excludes most of the known particles. The neutrino is the only possible candidate for dark matter within the Standard Model due to its weak interactions. Yet, the neutrino's small mass scale means it fits into the category of hot dark matter. On the other hand, Cold dark matter candidates are often preferred because their extensive mass range (from GeV to TeV) aligns well with the structures observed in galaxies [1].

1.2.1 WIMP

WIMPs are potential dark matter candidates. After the inflationary period, the universe reached a high temperature and density, allowing the Standard Model particles and dark matter components to exist in a balanced thermal equilibrium. This meant that the Standard Model of particles could convert into dark matter particles through annihilation and vice versa.

$$\chi + \bar{\chi} \longleftrightarrow SM + S\bar{M}, \tag{1.4}$$

where SM represents standard model particles, and χ denotes a dark matter particle. In the universe's early stages, the temperature (T) was so high that dark matter particles were moving at relativistic speeds, where T was significantly greater than the dark matter particle's mass. At this time [17]:

$$n_\chi(T) \propto T^3, \tag{1.5}$$

where n_χ in Equation 1.5 represents the density of dark matter particles. By using the Boltzmann constant, which relates temperature to molecular kinetic energy, we can express temperature in electronvolts (eV), similar to how we express mass. If the universe were static, these reactions would stay balanced. However, a significant shift occurs in an expanding and cooling universe when the universe's temperature drops below the dark matter particle's mass, $T < m_\chi$. At this point, dark matter particles transition from being relativistic to non-relativistic, thus [18]:

$$n_\chi(T) \propto e^{-m_\chi/T}, \tag{1.6}$$

where this exponential factor in Equation 1.6 is due to the decrease in dark matter production. As a result, the expansion rate eventually surpasses the annihilation rate, causing the two types of particles to exit thermal equilibrium. This phase, known as "WIMP freeze-out," marks the moment when the density of dark matter per co-moving volume becomes so low that the likelihood of two dark matter particles interacting becomes negligible compared to the expansion of the Universe. Consequently, at the time of WIMP freeze-out, the total number of dark matter particles in the universe became constant.

SuperWIMPs is a lighter variation of a WIMP. The hypothesis suggests that their interactions are so weak that they can be comparable to gravitational interactions, which are extremely weak relative to other fundamental forces. They are categorized as warm dark matter due to their lower mass compared to cold dark matter and their more relativistic behavior. Their particle cross sections are incredibly small, making it unlikely for them to have achieved thermal equilibrium in the early Universe. Instead, it's suggested that these particles might have originated from the decay of heavier nuclei, possibly including the decay of WIMPs.

Axions, another well-motivated dark matter candidate, arise from solving the strong CP problem in physics. This problem questions why the strong interaction doesn't naturally violate CP symmetry but maintains it. If axions don't exist, a fine-tuning in the Standard Model must occur. Axions are incredibly light (less than an eV). Despite their small mass, axions have properties that make them behave as cold dark matter. Their unique characteristics make axions an intriguing dark matter candidate [19].

Even though all these options are potential candidates, the DEAP-3600 experiment and, consequently, this thesis will centre on WIMPs. Therefore, any mention of "dark matter" moving forward refers to WIMPs.

1.3 Experimental Methods for Dark Matter Detection

Detecting dark matter, including WIMPs and other potential dark matter particles, proves challenging due to the defining characteristic of low cross section. After decadeslong efforts by physicists in pursuing WIMP particles, WIMPs with cross sections around 10^{-45} cm^2 and masses about $100 - 1000$ GeV have been ruled out [20, 21]. Furthermore, inconsistencies among published results have failed to obtain agreement within the scientific community regarding any definitive discovery of WIMPs. The search for dark matter spans three approaches: search dark matter in particle colliders, direct detection, and indirect detection, as illustrated in Figure 1.4.

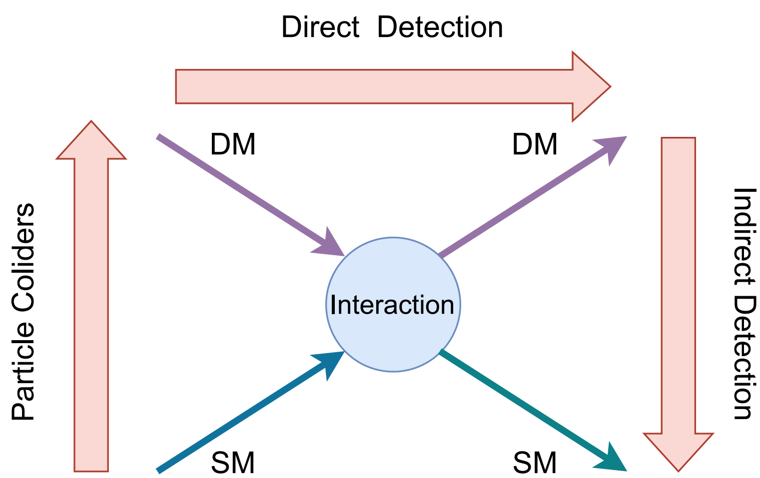

Figure 1.4: A schematics illustration of the three approaches employed in experimental dark matter searches: particle colliders, indirect detection, and direct detection. This thesis emphasizes the direct detection channel.

In the particle collider method, two extremely high energy standard model particles (energy order of TeV) collide to produce dark matter particles, similar to what happened in the early universe. The ATLAS and CMS experiments at the Large Hadron Collider are trying to observe these interactions [22]. These experiments can't directly detect the produced dark matter particles using their components. Instead, these particles lead to what's known as missing energy. In many analyses, most missing energy is due neutrinos, which don't leave any trace in the detectors [23].

Indirect detection aims to uncover any traces of dark matter decay or self-annihilation, as shown in Figure 1.4. If dark matter passes through a star, like the Sun or any large star, it may scatter off atoms and subsequently lose its energy. If the energy loss becomes high enough, it could gravitationally bind to the star, increasing the density at the star centre and thereby enhancing the likelihood of annihilation. While photons might not escape these objects, neutrinos commonly do. Experiments with goals to optimize neutrino sensitivity, such as SuperKamiokande and IceCube [24, 25], could detect this flux, potentially signaling the presence of dark matter. Additionally, the Galactic centre serves as a key region for searching for dark matter annihilation due to its high dark matter density. Gamma-ray observatories like FERMI-LAT have been critical in probing this region, looking for excess gamma-ray emissions that may indicate dark matter self-annihilation [26].

In direct detection, the idea is to use a material as a target to interact elastically with dark matter. When a WIMP interacts with a nucleus, the resulting evidence may appear as heat, charge, or scintillation light. This information helps differentiate between a potential WIMP scatter and background events. Removing background is crucial in this method, presenting a challenge for these types of detectors. Hence, these detectors are built underground to reduce background from cosmic and other sources.

In dark matter research, various experiments use different methods to fully explore the WIMP parameter space. The parameter space for multiple experiments is visible in the figure below. The lines in Figure 1.5 show exclusion curves at the 90% confidence level for some significant WIMP experiments. The yellow-shaded line denoting the neutrino floor in the figure limits the parameter space. In this zone, events of neutrino-nucleus scattering become an unavoidable background because they can't be distinguished from WIMP-nuclei interactions. This background notably decreases WIMP sensitivity, marking the boundary of the WIMP direct detection parameter space. The reason we don't see the indirect exclusion curve on the same plot is that the indirect dark matter cross-section is several orders of magnitude less precise and highly model-dependent.

Direct detection experiments can use one or a combination of three methods: charge, scintillation, and heat. Figure 1.6 displays the current exclusion curves from experiments focusing on spin-independent interactions, where interactions are not affected by the spin of particles. Instead, these experiments target overall mass and charge distributions. The exclusion curves represent the WIMP-nucleon cross section as a function of WIMP mass.

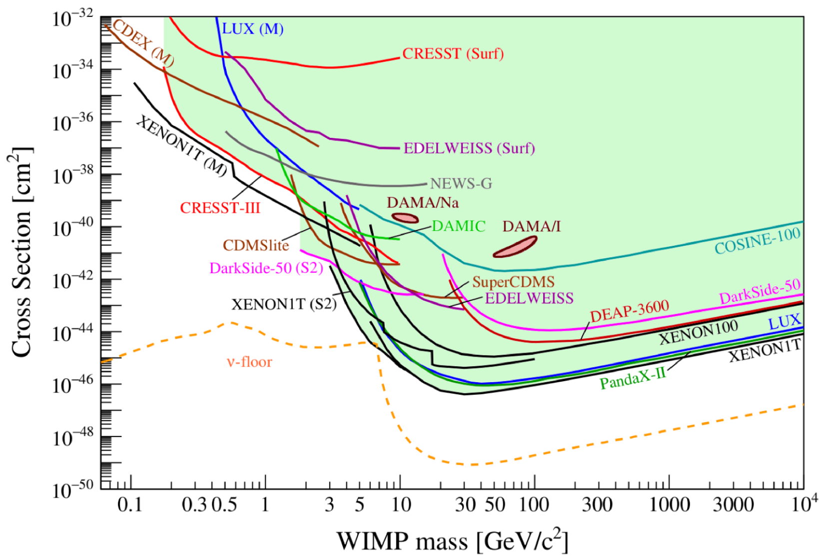

Figure 1.5: Exclusion curves at the 90% confidence level for spin-independent WIMP interactions with atomic nuclei in different experiments. Below the orange dotted line is where the background from coherent neutrino scattering becomes an irreducible background [2].

Different experiments employ one or two of these techniques and various target media.

An example of detectors using heat and charge is SuperCDMS. SuperCDMS relies on Silicon and Germanium crystals as its target media. To reduce the thermal background created by the crystals, they are kept at a low temperature of 15 milliKelvin [28].

DarkSide-50 (using argon) [29], LUX [30], XENON1T [31], and PANDAX-II [32] (using xenon) are detectors that use noble liquids and operate in a dual-phase time projection manner. They apply an electric field to the scintillation material, enabling the acceleration of electrons and generating a secondary scintillation signal alongside the primary one in the noble liquid. By combining these signals with event charge, they can reconstruct the event's position. In contrast, DEAP-3600 stands apart from the others as it operates differently—it's a single-phase liquid argon detector without an electric field in the chamber. This means it only uses a scintillation signal from the liquid scintillator. DarkSide, as a dual-phase time projection chamber using noble liquids, is a detector capable of measuring both the scintillation light induced by particles interacting in the active noble liquid target and the ionization charges produced during the event. In the

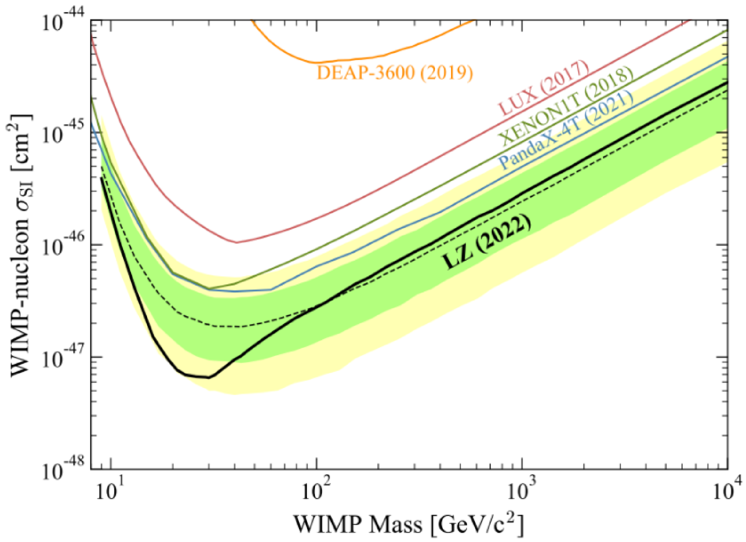

Figure 1.6: Current exclusion curves on the spin-independent WIMP-nucleon cross section based on the WIMP mass in different detectors with direct detection method. This image is from the DEAP-3600 publication, taken over 231 days of operation [27].

next chapter, we will discuss the DEAP-3600 detector in detail.

Chapter 2

DEAP-3600

DEAP-3600 is a single-phase liquid argon detector designed to directly detect WIMPs using scintillation light. This chapter will explain the details of the DEAP-3600 detector, including the physics behind the scintillation process, why liquid argon is used as the target material, and the design of DEAP-3600.

2.1 Noble Liquids

Noble liquid detectors rely on scintillation light to detect event signals. These noble liquid detectors have the advantage of utilizing a target material with commercial availability and inert properties [33]. Two of the most common target materials used in dark matter detectors are liquid xenon and liquid argon. The DEAP-3600 experiment utilizes 3279 kg $\pm$ 96 kg of liquid argon as its target material [34].

2.1.1 Scintillation Signal

WIMP particles passing through the target material can scatter with argon nuclei and deposit energy. DEAP-3600 is designed to capture the scintillation light from these interactions within it. A WIMP interaction with argon generates scintillation photons with a wavelength falling within the vacuum ultraviolet range, peaking at 128 nm [35]. The argon is transparent to these photons. There are two mechanisms for producing photons by argon: one is the process of excitons (excitation), and the other is ions produced by ionizing radiation (ionization) [36].

In the first case, after a WIMP particle scatters with an argon nucleus, one excited argon atom will remain (Ar^*). This excited argon atom can then bind with a ground-state argon atom to create an excimer (an excited argon dimer, Ar_2^*). This excimer will return to the ground state, releasing a scintillation photon. The steps of this process are shown below:

$$\begin{aligned} Ar^* + Ar &\rightarrow Ar_2^* \\ Ar_2^* &\rightarrow 2Ar + h\nu(128nm). \end{aligned} \tag{2.1}$$

The process of ionization of argon is similar to the first case. After scattering, we obtain an ionized argon atom (Ar^+). This ionized argon atom can then bind with a ground-state argon atom to create an ionized dimer (Ar_2^+). The recombination of this ionized dimer with a free ionized electron produces a highly excited argon atom (Ar^{**}), causing the other argon atom to return to the ground state. The Ar^{**} atom will reach the lowest excited state, releasing energy in the form of heat. After this point, the same process as excitation occurs, resulting in the emission of a scintillation photon. The steps of this process are shown below [37]:

$$\begin{aligned} Ar^+ + Ar &\rightarrow Ar_2^+ \\ Ar_2^+ + e^- &\rightarrow Ar^{**} + Ar \text{ (Recombination)} \\ Ar^{**} &\rightarrow Ar^* + \text{ heat} \\ Ar^* + Ar &\rightarrow Ar_2^* \\ Ar_2^* &\rightarrow 2Ar + h\nu(128nm). \end{aligned} \tag{2.2}$$

The ratio of scintillation light to incoming particle energy (light yield) is high for noble liquids [36]. DEAP utilizes this advantage to measure incoming photons by installing 255 PhotoMultiplier Tube (PMT)s around the detector. The detector is designed to collect the scintillation photons and convert them into PhotoElectron (PE). These PE values are stored for each event for analysis. Figure 2.1 summarizes these two mechanisms.

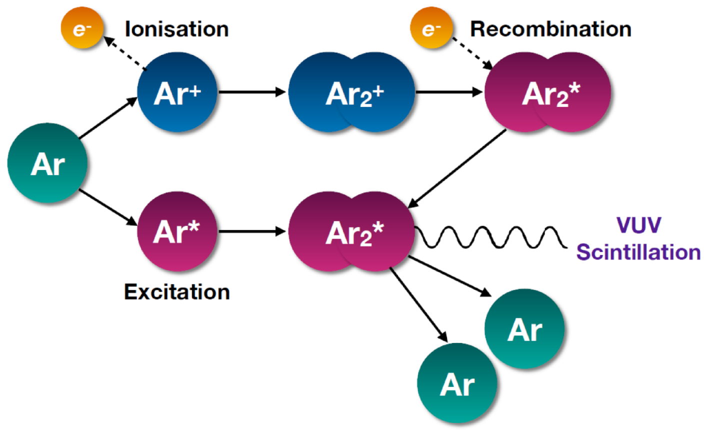

Figure 2.1: Illustration of two different mechanisms for producing photons from liquid argon: excitation and ionization [38].

2.1.2 Pulse Shape Discrimination

All the noble gases, including liquid argon, have similar light yields [36]. In DEAP-3600 detector, after accounting for PMT after-pulsing, this light yield is measured to be 6.1 ± 0.4 PE/keV [34]. In addition to this, argon can be extracted from the atmosphere, making it more accessible and lower in cost compared to other options like xenon [33]. However, the most compelling factor for choosing argon is its ability to achieve a high level of pulse shape discrimination, a crucial property in the design of DEAP-3600.

There are two different possible spin states for the excited dimers mentioned in the previous section, each with different lifetimes. The singlet state's lifetime is eight ns, while the triplet state has a much longer lifetime of 1.5 µs [39]. This significant separation between the two lifetimes makes liquid argon a better choice than xenon, where the separation between the two states is just a few nanoseconds.

All the events that occur within the detector can be categorized into two different categories: events that are initiated by electrons or gamma rays in liquid argon (Electro-Magnetic (EM)) and events that are initiated by energetic argon nuclei (Nuclear Recoil (NR)). EM events, such as β decay, produce more argon excimers in triplet states, leading to longer lifetimes. Conversely, NR events, such as WIMP scatters, produce more argon excimers in the singlet state, producing photons in a short time window. The

DEAP-3600 detector utilizes these advantages to define the variable Fprompt, the ratio of early light or prompt window (defined as the first 60 ns of the event) to the total light of an event (equation 2.3), we can distinguish between EM and NR events:

$$\text{Fprompt} = \frac{\sum_{t=-28ns}^{60ns} \text{PE(t)}}{\sum_{t=-28ns}^{10\mu s} \text{PE(t)}}. \tag{2.3}$$

The distribution of Fprompt for these two types of events is illustrated in Figure 2.2. EM events, characterized by the production of more triplet excimers, exhibit a peak around 0.3, whereas NR events, favoring singlet excimers, show a peak around 0.7. The distinction between these peaks is evident in the figure. Utilizing the Fprompt value enables the focus on NR events while efficiently rejecting background EM events.

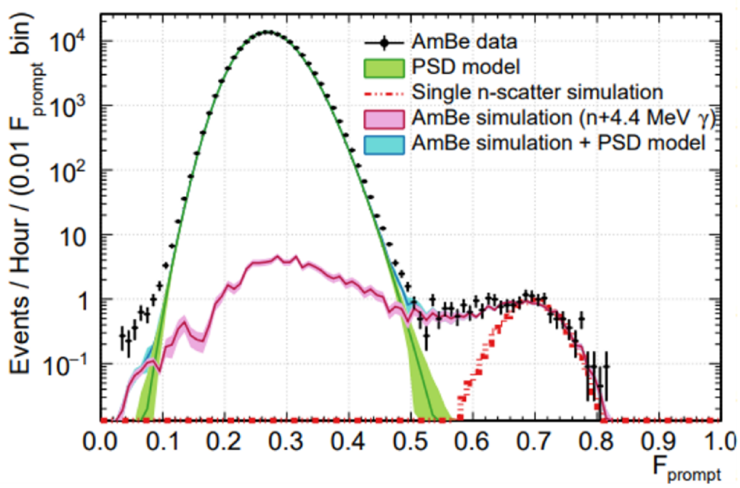

Figure 2.2: The distribution of Fprompt for events within the WIMP PE range (120-200 PE) is illustrated using data from the AmBe source [34].

Defining Fprompt enables us to establish a region of interest for WIMP searches, where sensitivity is maximized. In Figure 2.3, Fprompt vs PE shows the region of interest. The contour limits of the region of interest shown in Figure 2.3 serve to define background events. The lower bound helps define any EM events from the dark matter search. NR events (non-WIMP) can intrude into the region of interest, so it's crucial to understand these events and find the appropriate method to eliminate them. In the next chapter, we will talk about these attenuated alphas.

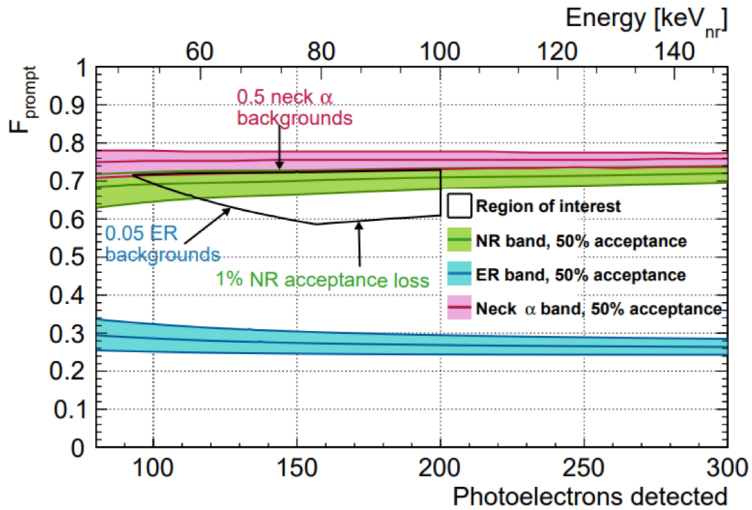

Figure 2.3: Fprompt vs PE for dark matter region of interest [34].

2.2 DEAP-3600

2.2.1 SNOLAB Facility

The ability to reduce the amount of cosmic ray muons is essential to any astroparticle physics experiment, so the location in mines is suitable for this purpose. The DEAP-3600 detector is located at the SNOLAB underground research facility. The SNOLAB facility was created at the Creighton Mine, roughly 2 km below ground, for the Sudbury Neutrino Observatory (SNO) experiment. This 2 km of rock heavily limits cosmic radiation, and this is very important for any neutrino or direct dark matter experiment, which needs to minimize all the backgrounds as well. The cosmic ray muon flux in SNOLAB was measured to be 0.27 muons/m^2/d [40]. The benefits of this limitation of cosmic rays are crucial despite limited accessibility to the detector during the construction and runtime. In Figure 2.4, the layout of the SNOLAB facility is shown. The DEAP-3600 detector is located at Cube Hall, indicated by a circle at the top left corner of the figure.

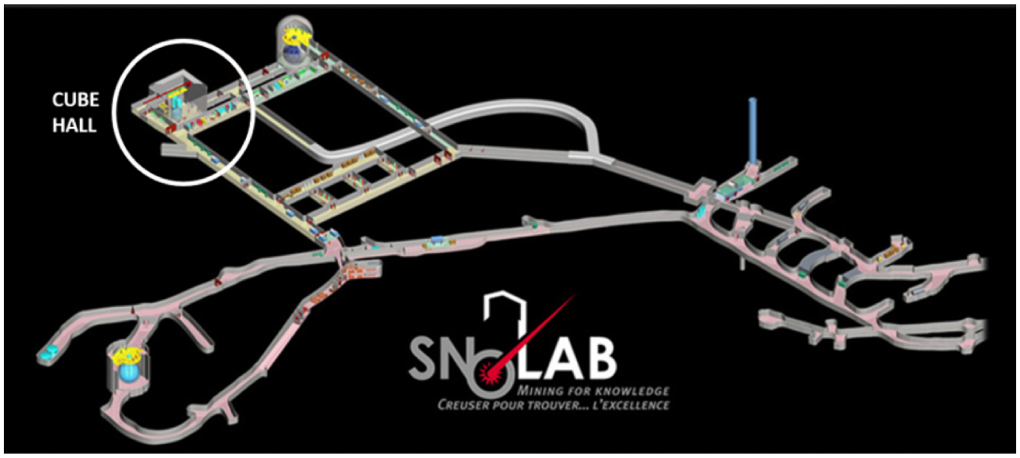

Figure 2.4: Layout of the SNOLAB facility. DEAP-3600 detector is located at the Cube Hall [40].

2.2.2 Detector Design

Figure 2.5 depicts a cross-sectional schematic of the DEAP-3600 detector. In this section, the detector components labeled in the figure will be described individually, starting from the innermost components and progressing outward. Finally, a brief explanation of the data acquisition. and the DEAP-3600 simulation software will be provided.

The Acrylic Vessel is 5 cm thick and has a radius of 851 mm. There are several reasons for choosing acrylic as the material. The optical and thermal properties of acrylic are crucial considerations in the detector design. The thermal conductivity of acrylic allows the significant temperature gradient between the liquid argon at 87 K, and the outer components can operate at room temperature. This temperature difference is substantial for exterior components such as PMTs, as they exhibit optimal efficiency at room temperature. Additionally, acrylic offers a well-controlled level of radiopurity and is manufactured to be as pure as possible [41].

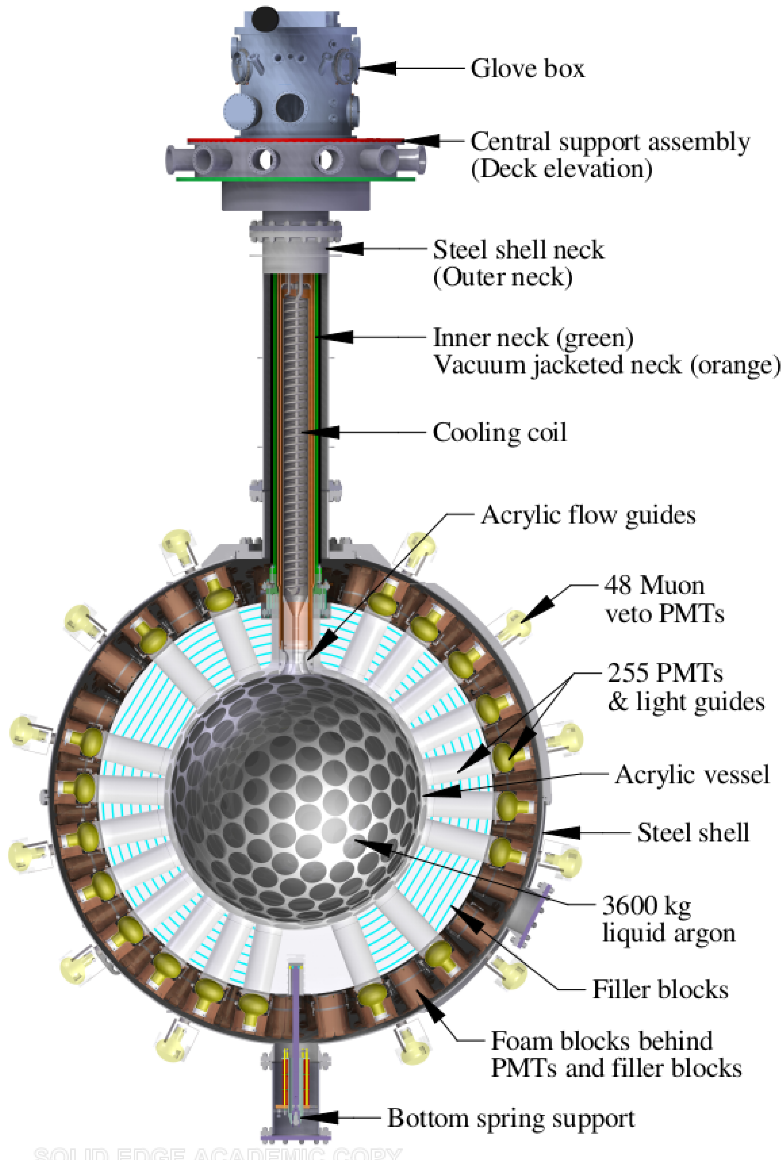

Figure 2.5: Cross-sectional schematic of the DEAP-3600 detector with labeled components [33].

At the top of the inner part of the detector, within the neck, there are two acrylic flow guides. These inner and outer flow guides are designed to shield the inner acrylic vessel from the scintillation light produced in the neck and to improve the flow of liquid argon, facilitating the upward movement of gaseous argon into the cooling coils. These cooling coils utilize liquid nitrogen to cool down the liquid argon. The neck, a vertical tube at the top of the detector with an inner diameter of 255 mm, is constructed from steel like the entire vessel, with the inner vessel accessible through the neck. The deck is also connected to the detector via the neck structure [33].

A different acrylic material compared to the flow guide and Acrylic Vessel (AV) was used to design light guides for a specific purpose. The primary objective of light guides is to transmit light to the PMTs using internal reflection, requiring a higher level of light transmission to maintain signal sensitivity. Additionally, the design of light guides allows more radioactivity compared to flow guides and AVs. Furthermore, light guides also act as additional thermal insulators to allow the PMTs to operate at their highest efficiency at room temperature.

Light emitted from the inner acrylic vessel is captured by 255 Hamamatsu R5912-HQE PMTs, known for their high quantum efficiency. According to the manufacturer, the quantum efficiency is approximately 23% at 400 nm [42]. These PMTs cover approximately 75% of the inner vessel, and their structure is shown in Figure 2.6. Each PMT is composed of a photocathode, a focusing electrode, a dynode stack, and an anode enclosed within a vacuum tube. When a photon strikes the photocathode, it liberates a photoelectron through the photoelectric effect. This photoelectron is directed towards the first dynode by the focusing electrode, where secondary electrons are emitted. With each dynode maintained at a higher potential than the previous one, the electric field accelerates ejected electrons toward the subsequent dynode, exponentially amplifying the total number of electrons across the dynode stack. Finally, upon reaching the anode, the accumulated electrons generate a sufficiently large current to produce an electrical pulse. The dynode stack typically comprises ten stages, yielding a gain factor of 10^7 for bias voltages ranging from 1500 V to 1800 V [42]. The PMTs are a significant source of neutron background.

The acrylic allows visible light to pass through but blocks ultraviolet light. Additionally, the maximum efficiency of the PMTs lies within the violet region of the light spectrum, with a rapid decrease observed in the ultraviolet range [42]. Organic TPB is used to coat the inner acrylic vessel. This coating layer absorbs and re-emits the wave-

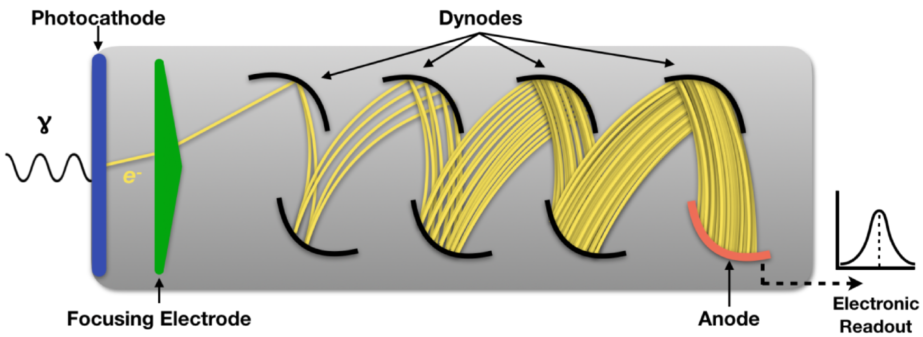

Figure 2.6: PMT dynode structure overview. Components include a focusing electrode, photocathode, dynode stack, and anode within a vacuum tube. Photon impact on the photocathode liberates electrons, leading to signal amplification across dynodes [42].

length of the scintillation light produced in liquid argon from ultraviolet to visible light (420 nm [43]). The TPB layer was applied via vacuum evaporation onto the surface, with a target thickness of 3 µm [44].

Polyethylene and polystyrene are used as materials for the filler blocks, which occupy the space between the light guides. These filler blocks serve as thermal insulation and neutron shielding in the detector regions between light guides. The entire setup is encased in a steel shell, further surrounded by an ultra-pure water tank. Despite the location of the detector at SNOLAB resulting in a low-level cosmic muon flux, it is not zero. To mitigate the remaining muon flux, 48 outward-facing Hamamatsu PMTs are positioned to cover the steel shell. We filter out events that coincide with Cherenkov light occurrences in the water tank. The figure below illustrates two stages of the inner detector construction with the described components.

The data acquisition system is responsible for capturing signals from the PMTs. In Figure 2.8, components of the DAQ are shown alongside a flowchart depicting the signal path through each component. This flowchart begins with photons being converted by the PMTs into an analog signal. Before reaching the digitizers, this analog signal undergoes shaping and preparation by signal conditioning boards (SCBs). The charge from these boards is measured using CAEN V1720 digitizers, resulting in a digitized trace of the PMT signal with a precision of 12 bits, equivalent to 4096 ADC (analog to

(a) Acrylic undergoing assembly with PMTs and filler blocks.

(b) Completed acrylic vessel with light guides

Figure 2.7: Illustration depicting two stages of the inner detector construction. Image courtesy of the DEAP collaboration.

digital) units. Additionally, the DAQ utilizes the CAEN V1740 as a low-gain digitizer in cases where the V1720 digitizer exceeds its 12-bit range due to a large amount of charge being sent from a PMT. These low-gain digitizers can record the data for these events. When a trigger is generated, digitizers will save a waveform within a time window of 16 ms. The digitizer and trigger module will use the summed signal from the signal conditioning board and trigger conditions to determine if an event generates a trigger. Subsequently, the digitized data and triggering information are passed onto an event object through the Event Builder software and then stored on disk.

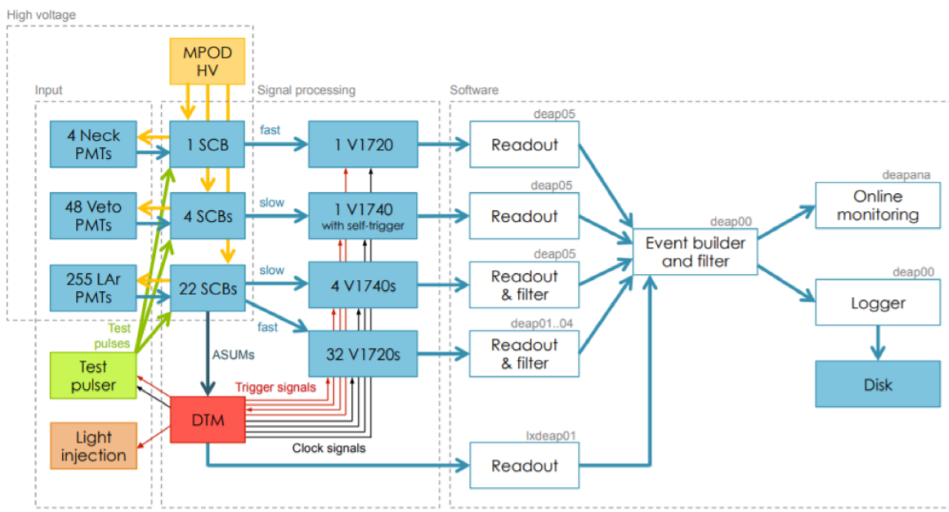

Figure 2.8: Illustration of DAQ system capturing signals, with components shown alongside a signal path flowchart. The process involves signal conditioning, digitization using CAEN V1720 and V1740 digitizers, and event triggering, leading to digitized data on disk storage. [45].

Chapter 3

Background Review in DEAP-3600

One of the main challenges faced by the direct detection method is the removal of background. This task holds great importance in the design of DEAP-3600. Considerable effort has been dedicated to constructing the detector to minimize background, primarily by placing it underground to minimize muon flux and using various materials for neutron shielding. However, specific background sources can produce events near the dark matter ROI. Based on the WIMP-simulated acceptance, the design goal of DEAP-3600 was to keep background events below 0.6 in the region of interest over a 3000 kg-year exposure. The target value of 0.6 was decided at the beginning of the DEAP design process. Considering a Poisson likelihood, this corresponds to a 55% chance of observing zero background events. This background level is not equally distributed among electromagnetic backgrounds, alphas, and neutrons [33]. This chapter will discuss key background types, including ^{39}Ar β-decays, neutron scatters, Cherenkov radiation, and α-decays.

3.1 ^{39}Ar β-decays

In DEAP-3600, there are various electromagnetic sources, which are shown in the Figure 3.1. In the top plot, the Fprompt versus PE is shown. The LAr alphas appear in the upper band, while the GAr band is characterized by Fprompt values near zero. The bottom plot displays the corresponding energy distribution for events within the ER band. Among these sources, ^{39}Ar is the most dominant. The liquid argon used in DEAP contains a small amount of ^{39}Ar from the air, which is unstable and can decay into ^{39}K with a half-life of 269 years [46]. When ^{39}Ar decays, it emits electrons into the scintillation material. These electrons then ionize argon in the detector, resulting in ER events in the detector. The rate for this background turns out to be 3000 Hz.

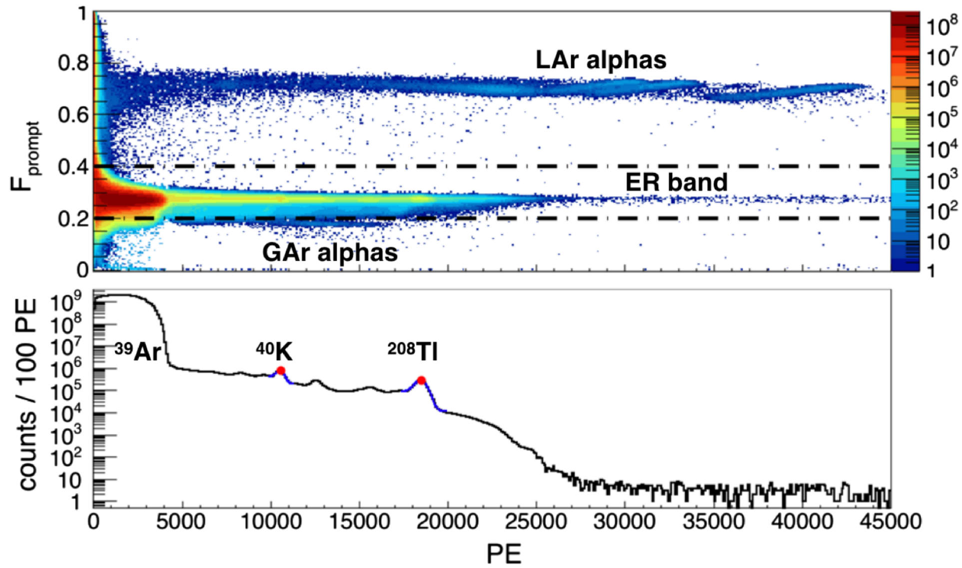

Figure 3.1: Top plot: Fprompt versus PE distribution of the 247.2 live-day dataset after a sequence of cuts with the LAr alpha band in the high Fprompt region and the GAr alpha band near zero. The lower plot shows the energy distribution of various event types within the ER band [47].

The choice of liquid argon was mainly due to the potential for pulse shape discrimination. As we can see in the Figure 3.2, this discrimination allows for rejecting electronic recoils in the dark matter search while accepting only nuclear recoils, as WIMP nuclei scatter. However, the reason that we are concerned about ^{39}Ar is not only its high rate compared to other sources, but for lower energies, the Fprompt distribution from these events widens, as can be seen in Figure 3.2. In this figure, the ^{39}Ar β-decays at low PE leak into higher Fprompt values. This spread comes from statistical fluctuations in the Fprompt measurement, as these low PE events have fewer photons detected. At higher energies, ^{39}Ar is well separated from nuclear recoil.

The upper band in the figure, NR events originate from various sources, except those related to ^{39}Ar. The reason for emphasizing ^{39}Ar events is the ability of other sources to generate sufficient energy (greater than 5000 PE), allowing their distinction through

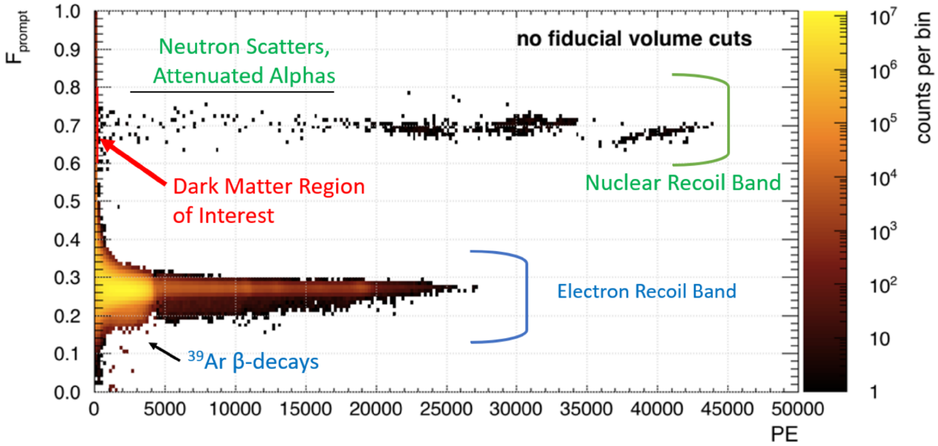

Figure 3.2: PE versus Fprompt for the 4.4 live-day dataset. The dark matter ROI, placed within the 80-200 PE range, is highlighted in red. The blue colour represents the EM band, while the green indicates the NR band. Graph courtesy of Phillip DelGobbo.

pulse shape discrimination. Therefore, they do not impact the dark matter search.

3.2 Neutron Scatters

Controlling neutron background is essential in the dark matter experiment. Due to their ability to cause nuclear recoils, they can behave similarly to WIMP signals. There are two general categories for neutron sources. The first one originates from cosmic ray interactions. The fact that SNOLAB is located 2 kilometers underground is essential for reducing this type of neutron. Any neutron surviving through these two kilometers of rock will be removed through the muon veto system.

The second source involves radiogenic neutrons caused by radioisotopes diffusing within and around the detector's components. The first source for these types of neutrons is the spontaneous fission of ^{238}U, while the other involves (α, n) reactions induced by the α-decay of the ^{238}Th, ^{235}U, and ^{238}U decay chains. (α, n) decay predominantly occurs within the borosilicate PMT glass and the filler blocks surrounding the detector. Acrylic light guides serve a dual purpose in addition to light transmission: they act as thermal shielding between the LAr and PMTs while also shielding against neutrons; this is important for meeting background specifications. The length of the light guides was chosen to prevent neutrons released from (α, n) reactions in the PMT glass from entering the WIMP ROI. This extended path length thermally slows down the neutrons, lowering their energy below the WIMP ROI threshold. All these precise design considerations effectively minimize the neutron background, staying within the set background level [34].

3.3 Cherenkov Radiation

If a particle moves through a medium at a speed greater than the phase velocity of light in that medium, it can produce Cherenkov light. This phenomenon can occur in an acrylic light guide within the DEAP detector. In most cases, the light resulting from this interaction is generated in a single light guide, and the attached PMT sees the light. Therefore, the Fprompt should be close to or equal to one. Thus, pulse shape discrimination helps us distinguish these events.

However, there are some cases where Cherenkov events coincide with ^{39}Ar, resulting in a single event with a lower Fprompt. These events might occur in the dark matter ROI. DEAP collaboration has defined the variable fmaxpe to distinguish specific events. fmaxpe represents the ratio of light captured by the brightest PMT to the total light. As Cherenkov light occurs within the light guide, it passes through the PMT associated with that specific light guide. Effectively, the fmaxpe variable assists in efficiently filtering out these events. Since scintillation light is generally isotropic in liquid argon, this background is nearly negligible in the context of the dark matter search.

3.4 Alphas

One of the most important backgrounds in DEAP is alphas, which is this thesis's primary focus. Alpha events in the nuclear recoil band can mimic a WIMP signal. In the DEAP detector, alpha events are emitted by various sources of radioactive isotopes within the detector. The major sources of these radioisotopes in the DEAP-3600 detector are ^{232}Th and ^{238}U, which are radioactive elements that have existed since before the Earth's formation and they have long lifetimes [48]. The decay chains of these two sources are shown in Figure 3.3 and Figure 3.4. The most challenging isotopes from their decay chains are ^{220}Rn from ^{232}Th and ^{222}Rn from ^{238}U. These daughter nuclei can migrate from the material where their parent nuclei decayed. Radon, in particular, spreads into the surrounding air. Especially in rocks with primordial uranium and thorium, radon levels rise significantly. While the detector was designed to prevent radon contamination by using low-radioactivity materials and ensuring high radiopurity in the vessel and TPB, the assembly of its components occurred underground at SNOLAB. This process involved exposing the acrylic to the atmosphere within the lab's underground environment [41].

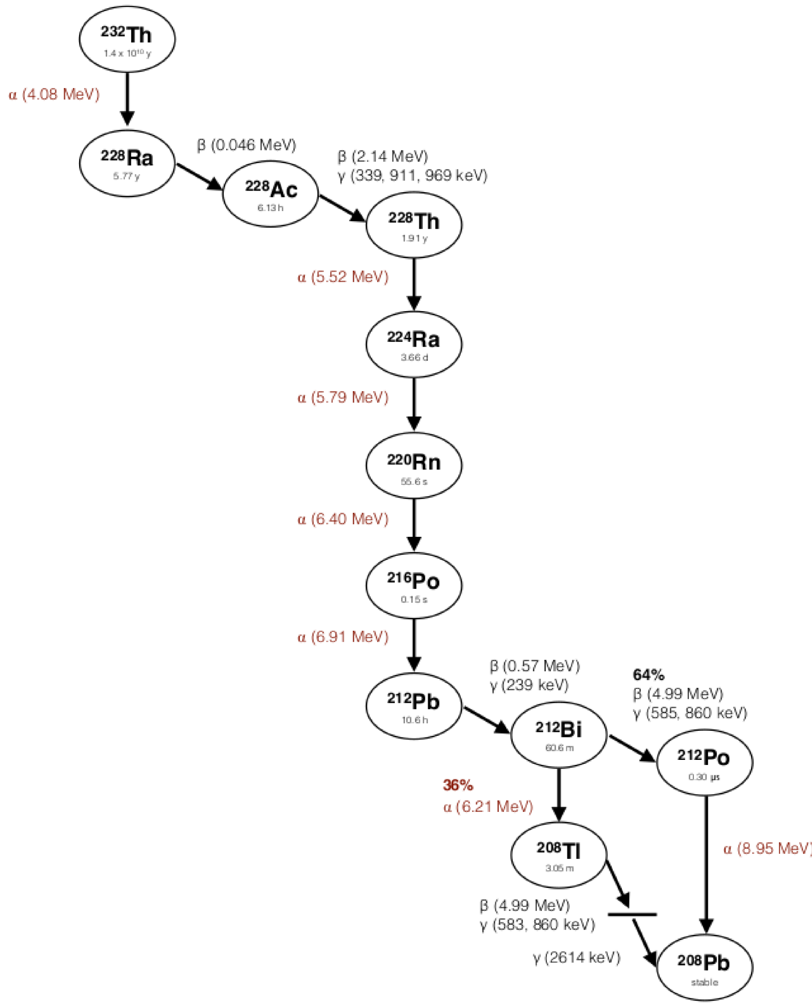

Figure 3.3: Decay chain diagrams of ^{232}Th [49].

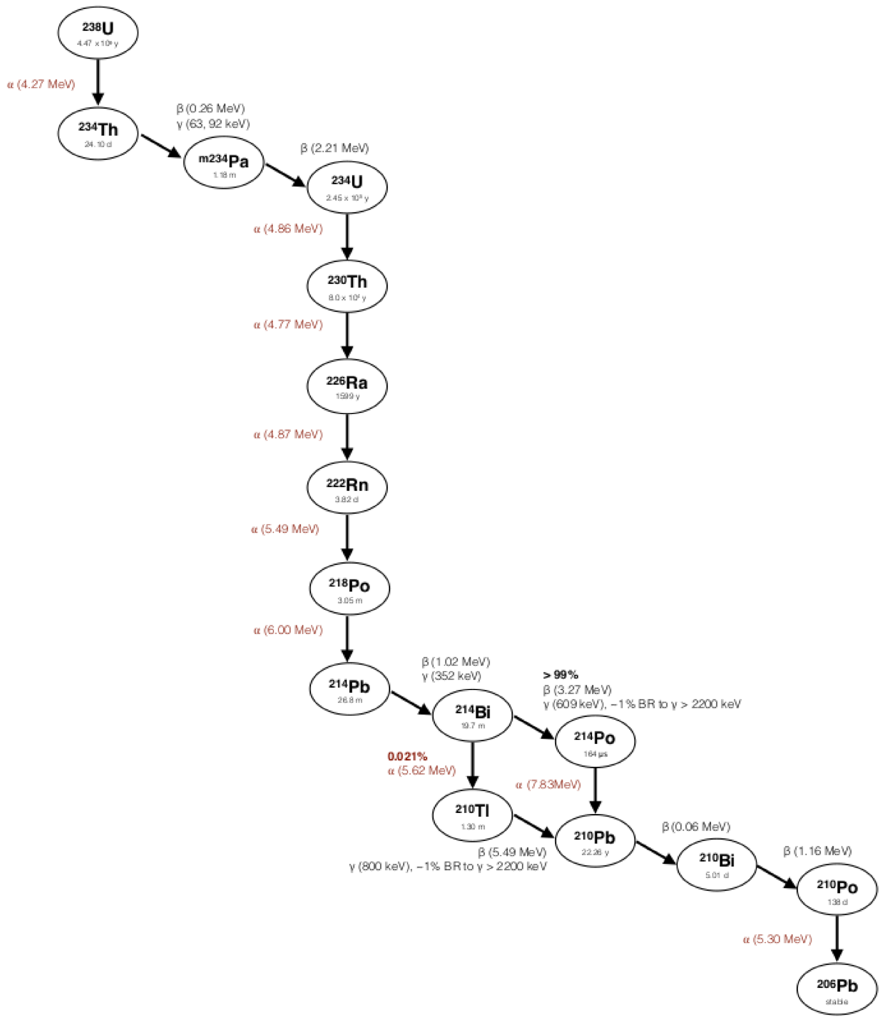

Figure 3.4: Decay chain diagrams of ^{238}U [49].

The decay chain of ^{220}Rn is illustrated in Figure Figure 3.3. It emits high-energy alpha particles within the liquid argon bulk. Its daughter nuclei, ^{216}Po and ^{212}Po, also undergo alpha decay. The decay sequence of ^{220}Rn ultimately leads to the stable isotope ^{208}Pb. ^{222}Rn, which can also emit high-energy alphas. The daughters of ^{222}Rn, ^{218}Po, and ^{214}Po also undergo high-energy alpha decay shortly after their parent's decay within the detector. however, observations reveal that ^{222}Rn and its daughters are the dominant alpha decay within the experiment [34].

The alphas from the discussed chains typically have high energy($>$ 20000 PE) in the MeV range and are often detected within the liquid argon. Therefore, they are easily distinguished from potential dark matter signal candidates under normal circumstances, whose energies usually fall within the 80-200 PE range. In Figure 3.5, we can see ^{222}Rn from a three-year dataset after applying specific cuts, along with its daughter isotopes emitting alphas within the DEAP detector. Notably, the energy range for full energy decays exceeds 20000 PE.

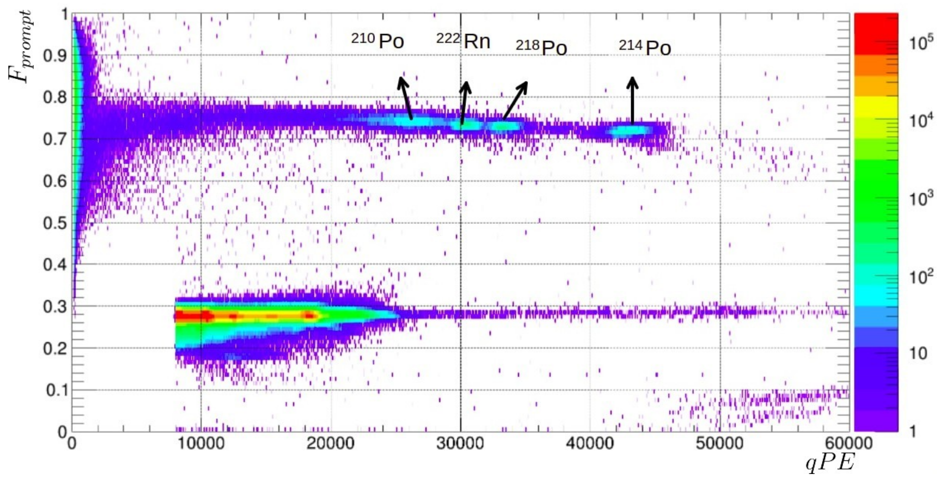

Figure 3.5: PE versus Fprompt for the three-year dataset. The colour bar represents the number of events, with colours ranging from 1 to 10^5. The cluster of ^{222}Rn and its daughters are depicted in this picture. The dark matter ROI falls within the nuclear band's 80-200 PE range.

There is a noticeable lower energy band in Figure 3.5 extending down from 20000 PE to zero. There are cases where alpha decays occur at less than full energies. There are three primary sources for these types of alphas. The first source is alphas emitted from the acrylic vessel's inner surface and TPB layer. Secondly, we have alphas originating from the acrylic neck flowguide surface. The last and most challenging one involves alphas occurring within dust particles, which is the main focus of this thesis. All three cases can lead to leakage into the WIMP ROI.

3.4.1 Alphas From Acrylic Vessel Inner Surface and TPB Layer

Among the various alpha sources with degraded energy, the ones occurring within the acrylic vessel inner surface and TPB Layer are the easiest to identify against the background. If an alpha decay occurs within the liquid argon, we have a full-energy alpha signal well above the ROI in the nuclear recoil band, making their removal straightforward.

However, Figure 3.6 demonstrates cases where alphas occur within the Acrylic Vessel or TPB. In the second situation, the alpha particle loses some energy within the TPB layer, generating TPB scintillation and resulting in a lower-energy degraded alpha or its daughter nuclei within the liquid argon. Depending on the depth of the initial position within the TPB, we can anticipate a spectrum of lower-energy degraded alphas.

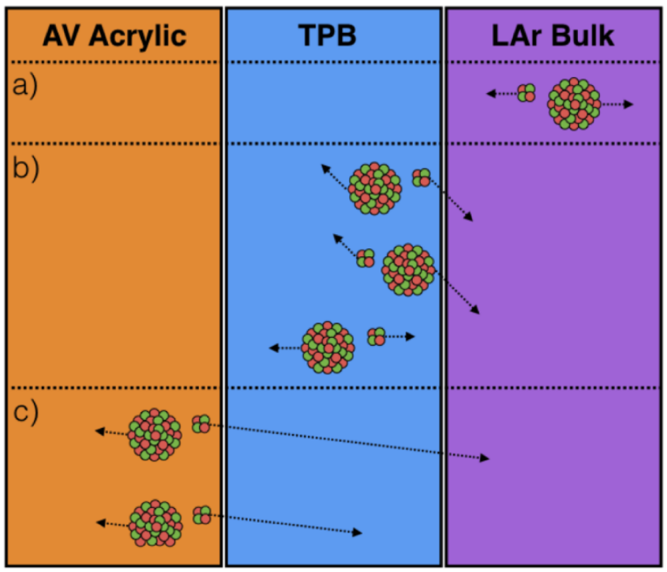

Figure 3.6: Illustration showing alpha interactions within the acrylic vessel, TPB layer, and liquid argon. Image courtesy of the DEAP collaboration.

In the second case, the alphas occur within the acrylic vessel, resulting in the loss of most of their energy within the acrylic vessel and the TPB layer. Consequently, this leads to another set of low-energy degraded alphas. Overall, these events can be effectively removed by implementing a fiducial requirement, enabling the removal of events close to the surface.

3.4.2 Shadowed Alphas

One of the most challenging background sources involves alpha particles within the acrylic flow guide of the neck (Figure 3.7). The neck, which is positioned at the top of the detector within the gaseous argon environment, is constructed with acrylic material. Like the inside of the acrylic vessel, the acrylic material in the neck can experience ^{210}Po decay. However, the critical distinction compared to the acrylic vessel surface lies in the geometry and shape of the neck structure. Alphas originating from this source will enter the gaseous argon region. A small amount of liquid argon exists within the flow guide through which these alphas pass, likely in the form of a thin liquid argon film.

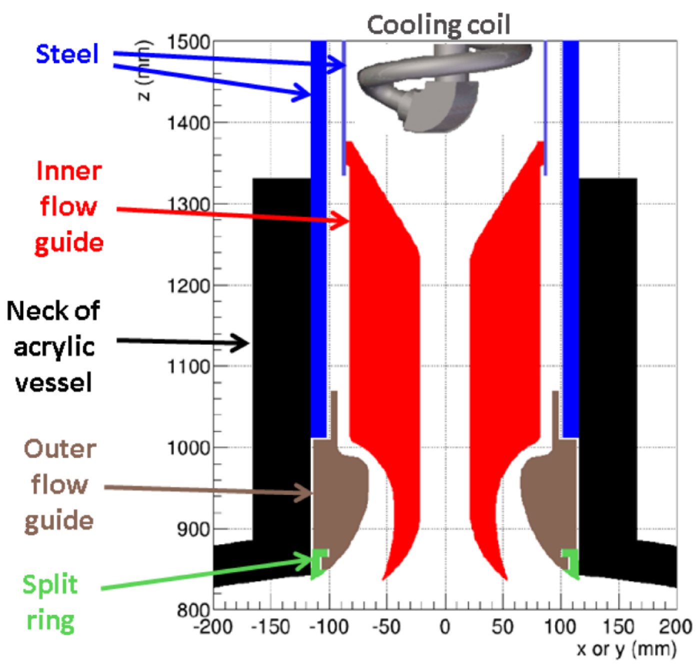

Figure 3.7: Illustration of the neck geometry. Image courtesy of the DEAP-3600 collaboration.

Alphas will generate scintillation light as they pass through this region of liquid argon. Due to the absence of a TPB layer on the acrylic flow guide, a significant portion of the UV scintillation produced by the alphas gets absorbed by other parts of the acrylic flow guide. This phenomenon, known as shadowing, reduces the number of scintillation photons, resulting in degraded alphas within the nuclear recoil band that can mimic the WIMP signal.

In the DEAP collaboration, a lot of effort is devoted to developing methods that help to mitigate this type of background, such as using machine learning algorithms [50] or likelihood approaches [51]. Despite all the efforts to reduce this background, it still represents one of the most significant portions in the WIMP background model of ROI [34].

3.4.3 Alphas From Dust Particulate Diffuse in LAr

In the figure below, we can observe how an alpha particle behaves within a dust particulate. If an alpha particle happens inside a dust particle, it will lose some energy before entering the liquid argon, carrying the remaining energy to initiate scintillation light. Some of the photons remaining will be absorbed again by the dust, a phenomenon known as shadowing, causing further energy reduction.

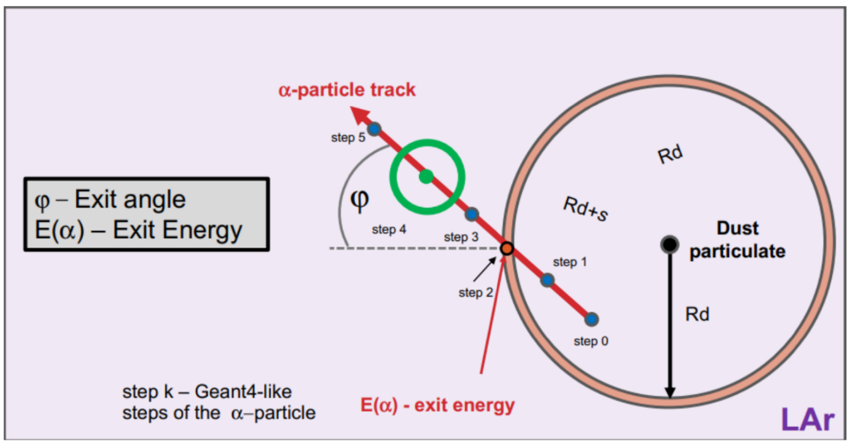

Figure 3.8: Illustration of the alphas from dust particles. Image courtesy of the DEAP-3600 collaboration.

This hypothesis suggests a wide range of energy for low-energy alpha particles. The assumption is that the positions of these degraded alphas are uniformly spread within the detector. Therefore, there is no fiducial cut to eliminate these backgrounds, such as for alphas originating from the inner surface of the acrylic vessel and the TPB layer. However, the question remains: Is there any evidence that supports the presence of such alpha particles?

The first evidence comes from the unexplained alphas with energy between 5000 and 20000 PE in the nuclear band. In the 231-live day results published, it was proposed that these unaccounted events could originate from dust particulate [34].

As a second piece of evidence, we can point to metallic dust. The presence of metallic dust within the liquid argon bulk is a potential concern. Erosion of metallic surfaces, especially in cryogenic liquid storage tanks may contribute to the generation of dust [33]. During resurfacing procedures, a 10-tonne nitrogen purge was employed within the vessel to mitigate radon activities. This involved passing the nitrogen through a 50 µm filter, allowing for the capture of dust particulates above this filter size. Dust samples were collected around the DEAP-3600 deck and detector floor and within the liquid nitrogen tanks. Analysis of the samples revealed the presence of copper and zinc dust residues in the liquid nitrogen using filter paper. These findings highlight the risk of metallic dust presence within the system.

But is there any proof of dust events in a data-driven approach? Before this study, there wasn't. So, the main focus of this thesis in the next chapters is to present this proof and discuss the properties of dust that we can observe in the data.

Chapter 4

Alphas from ^{214}Bi ^{214}Po Decay Chain

In this chapter, we will discuss the methods employed to identify the ^{214}Bi ^{214}Po decay chain in our three-year dataset, the largest unblinded dataset from DEAP to date. Subsequently, we will identify degraded alphas from this decay chain, explore their properties, and examine their potential connections to dust. We begin by defining some variables used in the DEAP-3600 analysis and employed in this study.

4.1 Cut Variables

In most DEAP-3600 studies, we employ specific cut variables to preprocess our dataset before proceeding with any analysis. These cut variables can be classified into two categories: low-level cuts and pile-up cuts. In this section, we will provide a brief overview of these two types.

4.1.1 Low-Level Cuts

Low-level cuts will help us remove any events impacted by instrumental effects.

- **dtmTrigSrc**: This cut will flag the source of the trigger in the detector. With this cut, we remove all internal periodic triggers or external calibration triggers and just focus on events with a physics trigger, defined as any event within the detector with PE > 20.

- **calcut**: There are multiple reasons for encountering bad events in the detector. Bad events may occur when the DAQ system is busy and suppresses the readout of the digitizers or when the high-gain V1720 digitizers exhibit a bad baseline. With the help of Calcut, we can identify and remove these types of events.

4.1.2 Pile-Up Cuts

With the help of pile-up cuts, we can eliminate suspicious coincidence events that involve more than one physical event in a single waveform or when there is any suspected light leakage from the previous event.

- **numEarlyPulses** ≤ 3: We use this cut to prevent any light leakage from previous events. This cut indicates that the number of pulses in the waveform for the first 1600 ns should be three or fewer.

- **2250 ns < eventTime < 2700 ns**: The eventTime measures the time of the initial pulse peak in an event relative to the start of the waveform. Typically, well-calibrated events occur around 2500 ns. To ensure data quality, the current data range is set between 2250 ns and 2700 ns. This range is applied to remove any trigger times occurring before or after the physics events. An event that is out of time indicates the detector was triggered by pile-up.

- **deltaT** $> 20\ \mu$s : DeltaT is the time interval between two events. We set a minimum range of 20 μs between consecutive events as a safety measure to prevent light leakage from previous events affecting the subsequent ones.

- **subeventN** $= 1$: By searching for more than one physics event occurring within a time window of 10 μs in the DAQ, we can determine whether the distribution of charges and pulses resembles that of a single flash of scintillation light or multiple flashes. The result of this search is called a subeventN, which is an integer corresponding to the number of suspected independent physics events within an event time window. Therefore, when the subevent equals 1, it suggests no indication of multiple pulses within the event waveform.

These six levels of cuts help us obtain a clean dataset with physics events for any study related to the DEAP detector. We refer to the combination of these six cuts as low-level cuts.

4.2 Calculated Variables

The primary data we have after any events in the Dark matter Experiment using Argon Pulse-shape discrimination (DEAP) detector are the digitized pulse voltages from 255 PMTs around our detector. We have multiple software processors that individuals use to generate these variables based on their specific needs in their research. In this section, we will mention the variables used in this analysis.

- **$\mathbf{F}_{\text{prompt}}$**: F_{prompt} is the pulse shape discrimination (PSD) variable that helps us distinguish between EM and NR, especially for energies greater than 1000 PE.

- **PE**: Two event energy variables are available for our studies: qPE and nSCBayes. The qPE variable is simpler than nSCBayes as it requires only the counting of PEs in each PMT for the specific event. In contrast, nSCBayes uses a Bayesian analysis to remove AfterPulsing (AP).

- **fmaxpe**: The portion of charge in the brightest PMT relative to the total event charge yields a variable helpful in removing Cherenkov backgrounds, called fmaxpe.

- **MBL**: One of the most important pieces of information required for most analyses in the DEAP project is the position of the event. There are two main position fitters used for this purpose. One of them operates based on the timing of events obtained from all PMTs (TF2), and the other operates based on the charge of PMTs (referred to as MBL, named after Mikhail Batygov, a DEAP collaborator). Additionally, there is an ongoing study to implement a neural network approach as a third-position fitter in the future. However, in this section, we focus on MBL because it has better resolution for most events. The MBL relies solely on the spatial distribution of the charge integrated over the full 10 μs time window. With the assistance of the Nelder-Mead minimization approach, the MBL can determine the optimal position describing the spatial charge distribution. To achieve this, the MBL fitter calculates the likelihood $\mathcal{L}(\vec{x})$ at the test position $\vec{x}$ as follows:

$$\begin{aligned} \ln \mathcal{L}(\vec{x}) &= \sum_{i=1}^{N_{\text{PMTs}}} \ln \ \text{Poisson} \ (q_i; \lambda_i) \,, \\ \lambda_i &= \lambda_i \left(|\vec{x}|, \frac{\vec{x} \cdot \overrightarrow{r_i}}{|\vec{x}| \, |\overrightarrow{r_i}|}, q_{total} \right), \end{aligned} \tag{4.1}$$

where q_i represents the charge of PE in the ith PMT located at position $\vec{r}_i$, and λ_i denotes the expected PE charge calculated through Monte Carlo (MC) simulations. It is dependent on factors such as the position $\vec{x}_i$, the angle between PMT$_i$, the test position, and the total event charge.

4.3 Dataset and Cuts

The three-year dataset (the most available unblinded data within the DEAP collaboration) is used. 414.76 days of running time from the three-year dataset are open for studies, while the remaining run days are still blinded. Our primary focus is on extracting the ^{214}Bi-^{214}Po decay chain. We first need to clean our dataset using the variables described in the previous section to achieve this. In summary, we can see the list of these criteria and the reasons for their use in Table 4.1 below.

Table 4.1: List of cuts used to clean the dataset, with a focus on identifying the ^{214}Bi-^{214}Po decay chain.

Event Selection	Purpose
dtmTrigSrc&0x82 = 0	Remove Non-physics triggers.
calcut&0x31f8 = 0	Remove non-physics triggers.
numEarlyPulses <= 3	Remove pile-up events.
subeventN = 1	Remove pile-up events.
$2250ns <=$ eventTime $<= 2700ns$	Remove pile-up events.
deltaT $> 20\mu s$	Remove pile-up events.
200 <= qPE	Remove Cherenkov events.
fmaxpe< 0.4	Remove events with 40% or more light in one PMT to remove Cherenkov events.
$\mathrm{MBL}_Z < 550mm$	Events within the liquid argon

4.4 $\beta - \alpha$ Events

There are two activities known to be present in DEAP that should appear as correlated $\beta - \alpha$ events: ^{214}Bi and ^{212}Bi. The daughter nucleus, ^{214}Po has a 163.6 μs half-life and decays by emission of a 7687 keV α. The daughter nucleus, ^{212}Po has a 0.299 μs half-life and decays by emission of an 8784 keV α. These two decay chains are illustrated in Figure 3.3 and Figure 3.4.

We are not able to detect ^{212}Bi-^{212}Po in this study, primarily due to the short lifetime of 0.299 μs. As mentioned in Chapter 2, DEAP utilizes a 16 μs time window for event detection. If two subevents are detected within a one-time window, they are removed by the cut of SubeventN=1. Essentially, the short lifetime of ^{212}Bi-^{212}Po results in a SubeventN=2, which fails to pass the cut.

The following sections demonstrate that we can detect the ^{214}Bi-^{214}Po decay chain by employing an appropriate time window.

In Figure 4.1, qPE vs. F_{prompt} is shown for the entire three-year dataset after applying the list of cuts outlined in Table 4.1. In this figure, we define α and β events as follows:

- α: High Fprompt events from NR (i.e., events with Fprompt between 0.6 and 0.8).
- β: Low Fprompt events from ER (i.e., events with Fprompt between 0.18 and 0.4).

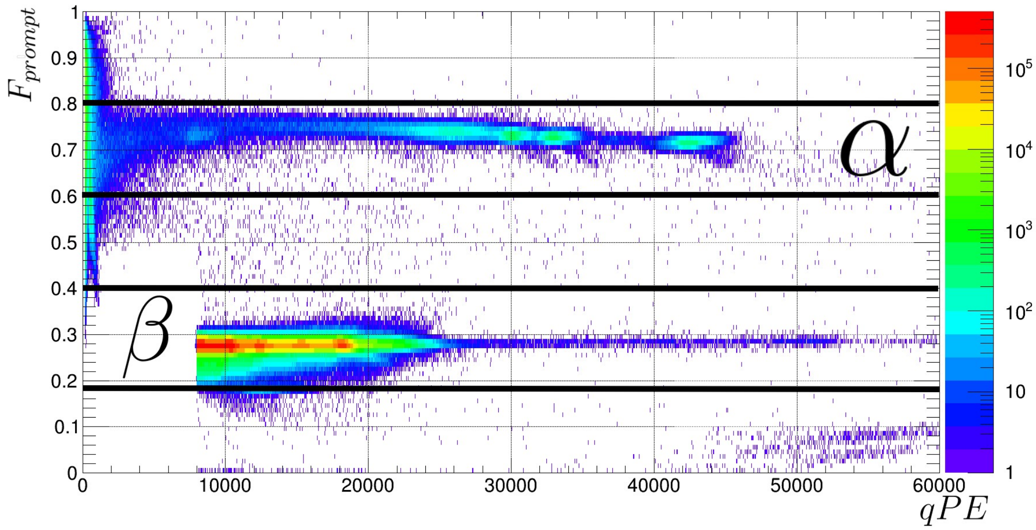

Figure 4.1: qPE vs. Fprompt for a three-year dataset after applying cleaning cuts. The colour bar represents the number of events, with colours ranging from 1 to 10^5. Definitions of variables α and β are provided in the figure.

For the next step, we need to find all $\beta - \alpha$ coincidences within a time window of 4 ms. The three-year dataset consisted of 47,492,040 events after applying the cuts in Table 4.1. We identified 13,481 $\beta - \alpha$ coincidences according to our definition (0.057% of all data).

The distribution of time differences between β and α is shown in Figure 4.2, along with a fit using the log-likelihood method. This distribution comprises two contributions: real $\beta - \alpha$ and accidental coincidences. If we denote the total number of $\beta - \alpha$ events as $N_{\beta-\alpha}$, with a decay rate λ, a bin width $t_{\text{bin}} = 10^4$ ns, a constant variable for accidental coincidences, we expect the distribution of times to be given by the following equation:

$$P(t) = N_{\beta-\alpha}\lambda t_{bin} e^{-\lambda t} + K \tag{4.2}$$

when we fit, we find:

- $N_{\beta-\alpha} = (132 \pm 2) \times 10^2$
- $\lambda = (4.20 \pm 0.04) \times 10^{-6} (1/ns)$

- $K = 2.32 \pm 0.01$

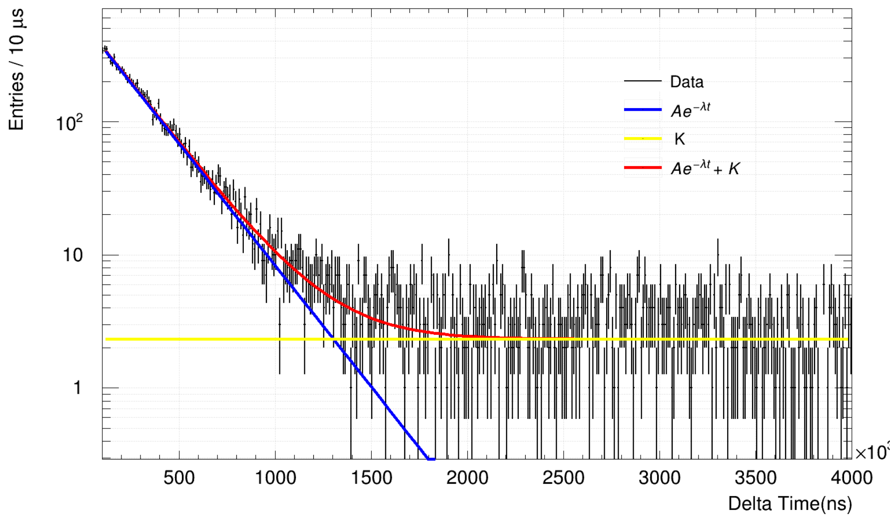

Figure 4.2: The distribution of time differences between β and α. The yellow line indicates the fit line for accidental coincidences, while the blue line represents the exponential fit for β and α coincidences.

Using the λ that we get from Equation 4.2, we can determine the half-life associated with the decay. Thus, the half-life calculation is as follows:

$$\frac{N(t)}{N_0} = \frac{1}{2} = e^{-\lambda t} \quad \Rightarrow \quad t_{1/2} = \frac{\ln 2}{\lambda} \quad \Rightarrow \quad t_{1/2} = 165 \pm 2(\mu Sec) \tag{4.3}$$

The calculated half-life of $165 \pm 2(\mu s)$ is consistent with the half-life of the ^{214}Bi-^{214}Po decay chain, as in Figure 3.4. Therefore, we can infer that the majority of events in Figure 4.2 originate from the ^{214}Bi-^{214}Po decay chain. Before examining the properties of these events, such as energy and F_{prompt}, we must reduce the rate of accidental events in our dataset. In the subsequent section, we will discuss an additional step aimed at improving the accuracy of our results.

4.5 ^{214}Bi-^{214}Po

Since the majority of events in Figure 4.2 originate from the ^{214}Bi-^{214}Po decay chain, these two events must come from the decay of a single nucleus that hasn't had time to move, so they should occur at the same position. We implement a cut on the MBL distance between any $\beta - \alpha$ coincidence to consider it a ^{214}Bi-^{214}Po candidate. In Figure 4.3, the MBL distance between $\beta - \alpha$ coincidences and their time differences is shown. After a distance of 400 mm between all $\beta - \alpha$ coincidences, mostly random events occur. Therefore, it seems reasonable to set a cut difference of 400 mm for any ^{214}Bi-^{214}Po candidate. By applying this cut, we lose 12.4% of the events, but we mostly eliminate accidental ones.

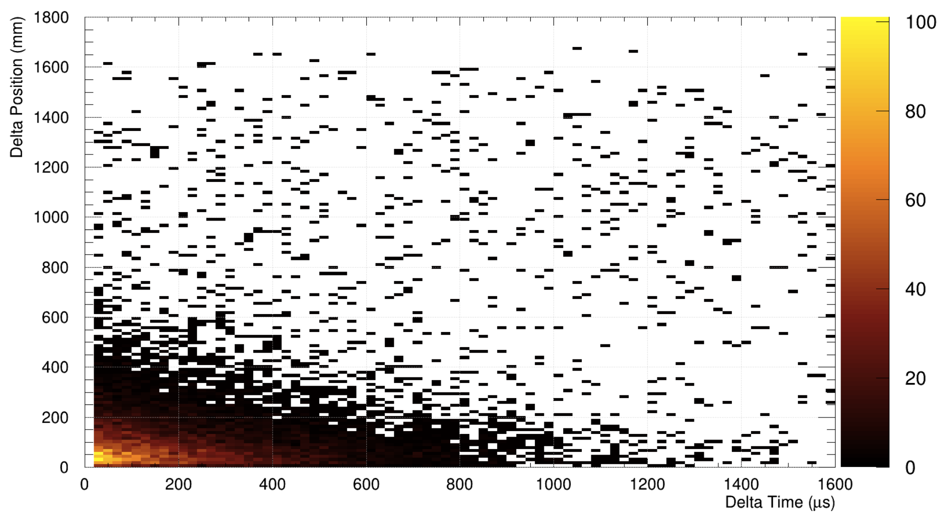

Figure 4.3: Distance vs. time difference for $\beta-\alpha$ coincidence. The colour bar represents the number of events, with colours ranging from 1 to 100. This figure demonstrates that events with distances greater than 400 mm predominantly correspond to random occurrences.

The step-by-step procedure for identifying ^{214}Bi-^{214}Po events is illustrated in Figure 4.4. This procedure detected 11,794 β-α coincidences within a 4 ms time window and a 400 mm distance. The distribution of time differences between β and α is depicted in Figure 4.5, along with a fit performed using the same method as that employed in the fitting process of Figure 4.2. The fit parameters of Equation 4.2 are detailed below:

- $N_{\text{BiPo}} = (125 \pm 2) \times 10^2$
- $\lambda = (4.40 \pm 0.04) \times 10^{-6} (1/ns)$

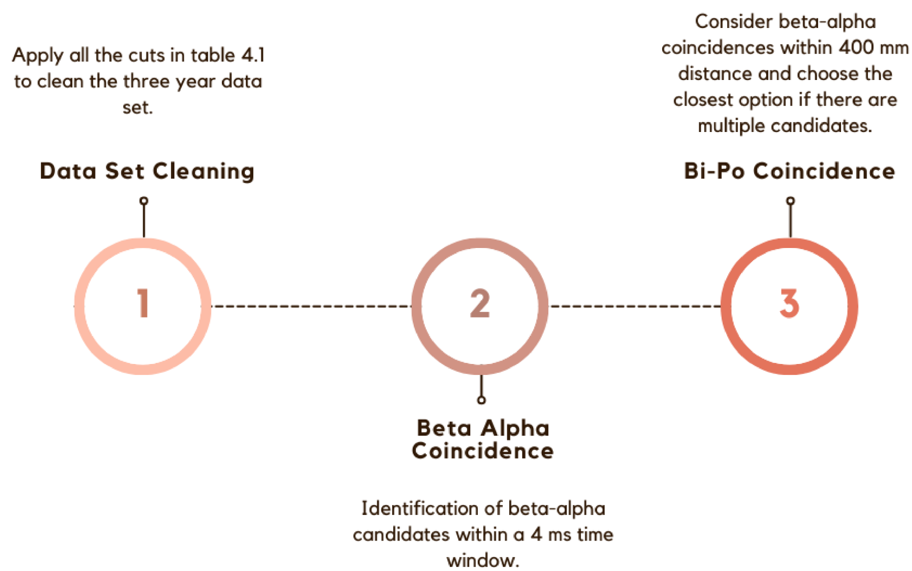

Figure 4.4: Flowchart illustrating the process for identifying ^{214}Bi-^{214}Po events, highlighting the sequential steps involved in the analysis.

- $K = 0.7 \pm 0.1$

Using the above λ, the calculated half-life associated with the decay is $t_{1/2} = 158 \pm 2\ \mu$s. This result indicates that incorporating the additional cut for identifying coincidences within the 400 mm range aligns the half-life with that of ^{214}Bi-^{214}Po while reducing the number of random coincidences.

One other aspect to check is the energy of β-α events. In Figure 4.6, the energy distribution is displayed alongside the 2D plot of Fprompt versus the energy of these events. A comparison between the energy distributions of α and β events reveals that β events(Figure 4.6d) exhibit a limited energy range, peaking at 15,000 qPE. In contrast, the alpha distribution(Figure 4.6c) spans a broader range of energies, starting from near zero and peaking around 42,000 qPE, consistent with the energy of the ^{214}Bi-^{214}Po decay chain. Additionally, comparing the 2D plot of Fprompt versus qPE reveals that alphas(Figure 4.6a) exhibit a more comprehensive range of Fprompt distribution at lower energies. The agreement of energy alongside the half-light can show that most of the β-α events found here are from the ^{214}Bi-^{214}Po decay chain.

In Figure 4.7, the positions of ^{214}Bi and ^{214}Po are displayed. The figure illustrates

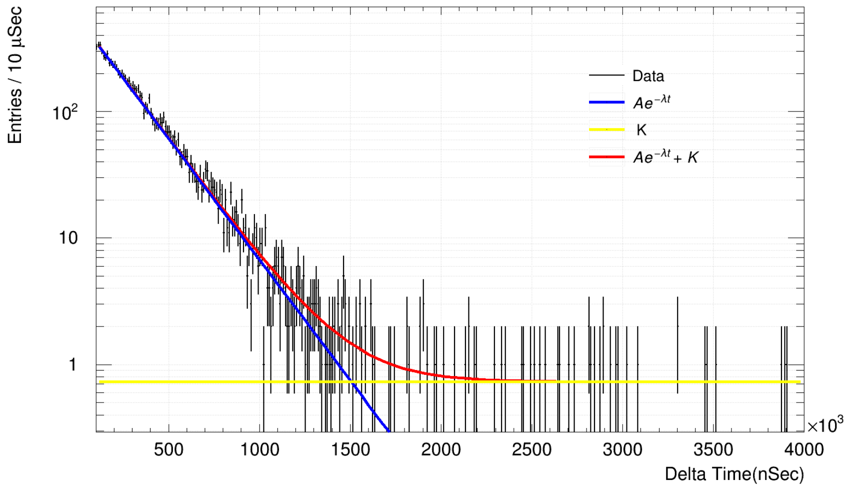

Figure 4.5: The time intervals between^{214}Bi and ^{214}Po events. The yellow line depicts the fitting curve for accidental coincidences, whereas the blue line illustrates the exponential fit for ^{214}Bi and ^{214}Po events.

a uniform distribution of positions within the detector, indicating an even spread of radioactive events. Moreover, the absence of clustering or localized peaks suggests that accidental events do not occur more frequently in specific regions of the detector. This uniform distribution is crucial for accurately assessing the characteristics of ^{214}Bi and ^{214}Po decay events, thus ensuring the reliability of the experimental data.

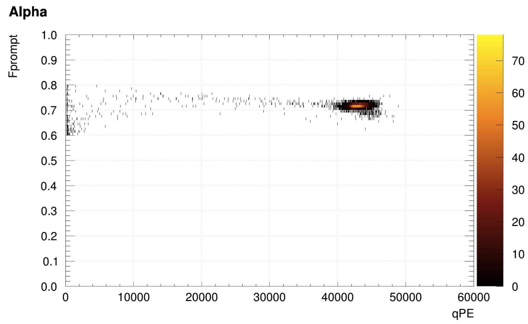

(a) α Fprompt vs qPE. The colour bar represents the number of events.

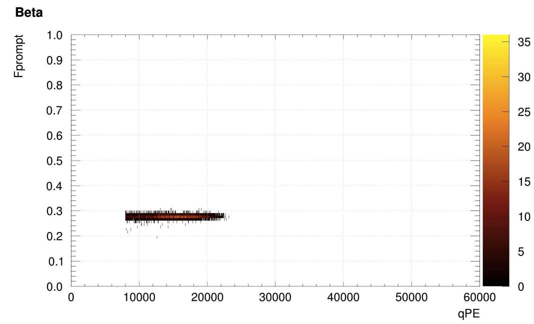

(b) β Fprompt vs qPE. The colour bar represents the number of events.

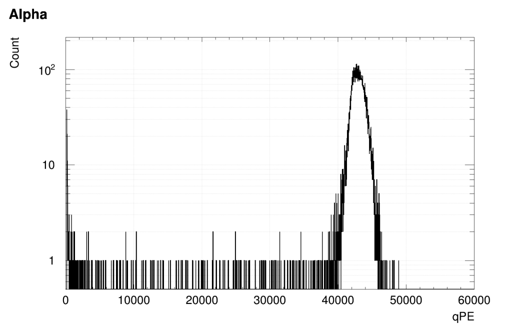

(c) Energy distribution of α events.

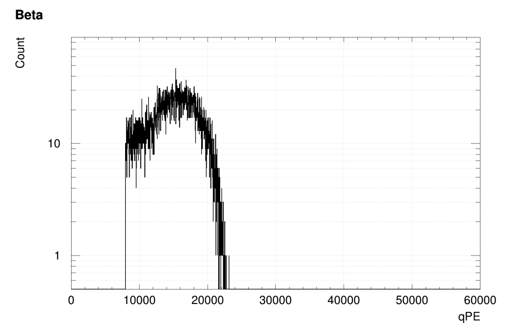

(d) Energy distribution of β events.

Figure 4.6: The comparison of energy distributions between α and β events reveals a broader range of α energies, starting from near zero, in contrast to the single peak observed in β events. Additionally, degraded alphas exhibit a wider range of Fprompt values at lower energies.

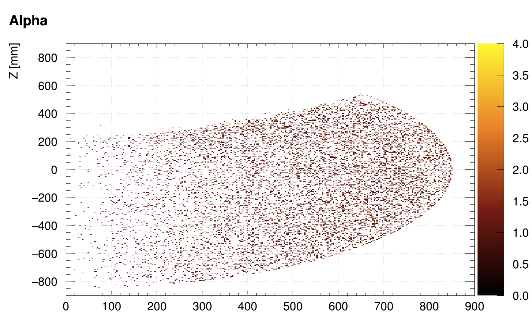

(a) Position of α events within detector. The colour bar represents the number of events.

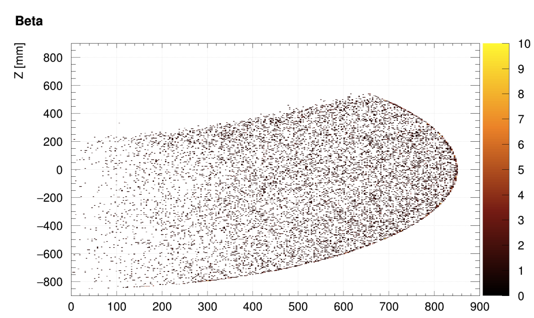

(b) Position of β events within detector. The colour bar represents the number of events.

Figure 4.7: The positions ^{214}Bi and ^{214}Po particles, show an approximately uniform distribution within the detector. There is a enhance for alphas at the surface.

4.6 Dust ^{214}Bi-^{214}Po

For events where ^{214}Bi is within the liquid argon, both α and β particles are expected to manifest at their full energies and be detected with 100% efficiency, except for a small fraction where nearly simultaneous events lead to a single electronics trigger. However, events occurring on the surface of the acrylic vessel may require particles to traverse non-scintillating material before detection. Since β particles have a much greater range than alpha particles, we anticipate that β particles will exhibit the same energy spectrum, while the energy of alpha particles may be significantly degraded. Additionally, we observe only half the events for surface events, reducing the probability of an α-β coincidence to 25% of the actual events.

In the case of dust events (section 3.4.3), it's expected that β particles will not undergo degradation, although alpha particles may. Here, we would also expect the efficiency to be 100% for both alpha and β particles. Consequently, we can categorize ^{214}Bi-^{214}Po events from the previous section into two categories:

- Dust ^{214}Bi-^{214}Po: Events with degraded alphas, defined as alphas producing less than 10,000 qPE and with a radius position of less than 845 mm.
- surface ^{214}Bi-^{214}Po: Events with degraded alphas, defined as alphas producing less than 10,000 qPE, and with a radius position greater than 845 mm.

By applying the condition for dust ^{214}Bi-^{214}Po events, we can find 24 coincidences with related time different time distributions shown in figure Figure 4.8. By applying the same approach of fitting as question 4.2, we can find:

$$P(t) = N_{\mathrm{BiPo}} \lambda t_{bin} e^{-\lambda t} + K, \tag{4.4}$$

where:

- $N_{\mathrm{BiPo}} = 28 \pm 3$
- $\lambda = (4.3 \pm 0.9) \times 10^{-6} (1/ns)$

- $K = 0.2 \pm 1.5$

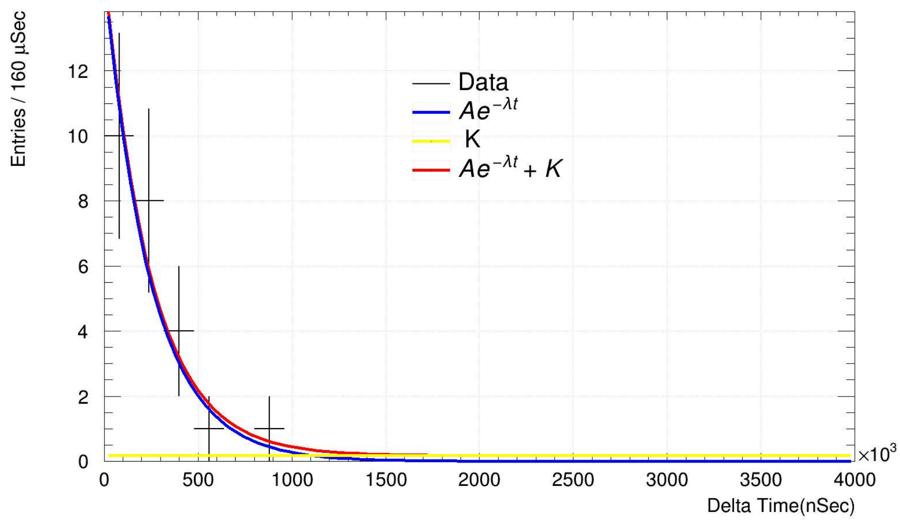

Figure 4.8: The time intervals between dust ^{214}Bi and ^{214}Po events. The blue line illustrates the exponential fit for these events, and the black bars show the related error bars calculated using a Poisson confidence level of 68%.

By using the λ from the above fitting equation, we can calculate the half-life as $t_{1/2} = 160 \pm 3$ μs, which agrees quite well with the half-lives of the ^{214}Bi and ^{214}Po decay chain. The distribution of energy for dust alphas is illustrated in Figure 4.9a by the red line, which exactly matches the cut we used for identifying dust events, alongside the black lines showing the energy of all alphas. Additionally, in Figure 4.9b, we observe the distribution of β particles related to dust alphas, shown in red, alongside the distribution of all β particles represented by the black line. This figure indicates that there is no specific energy range for β particles; instead, their energy distribution appears to be roughly uniform compared to that of all β particles. This result confirms our expectation that dust has no significant effect on β particles, but it suggests that all alphas may experience degradation.

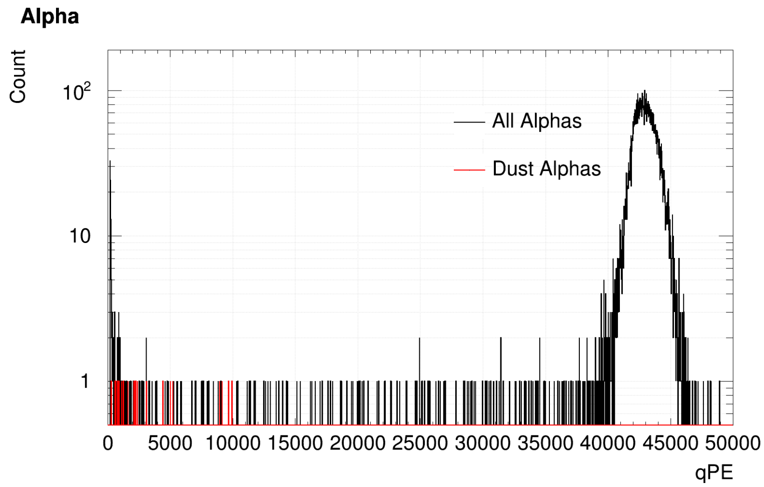

(a) Energy distribution of dust alphas (shown in red) and all alphas (shown in black).

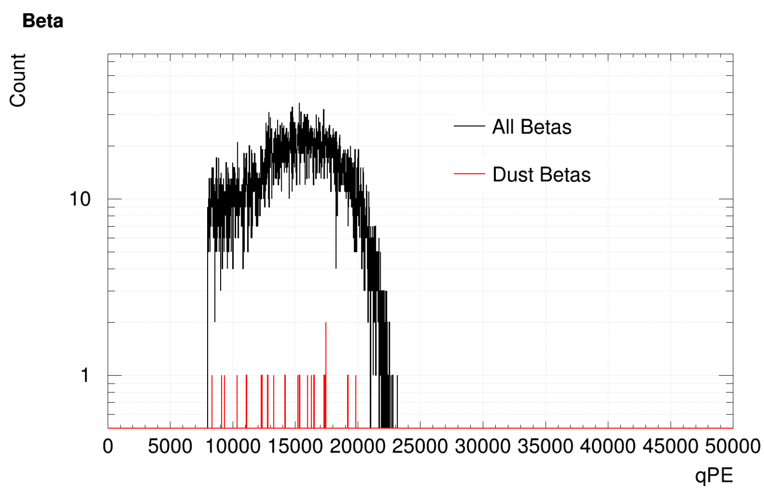

(b) Energy distribution of β particles related to dust alphas (shown in red) and all β events (shown in black).

Figure 4.9: Dust ^{214}Bi and ^{214}Po energy distribution alongside with ^{214}Bi and ^{214}Po. The uniformity in the energy distribution of β particles suggests minimal impact from dust, while indicating potential degradation in all alphas.

In Figure 4.10, the positions of the 24 dust ^{214}Bi and ^{214}Po particles are indicated by arrows representing the direction from ^{214}Bi to ^{214}Po. Further analysis conducted on the x, y, and z positions separately demonstrates that there is no specific region in the detector exhibiting clusters of dust events; instead, the positions are approximately uniform within the detector.

We expect that these 24 events occur approximately uniformly over the three-year

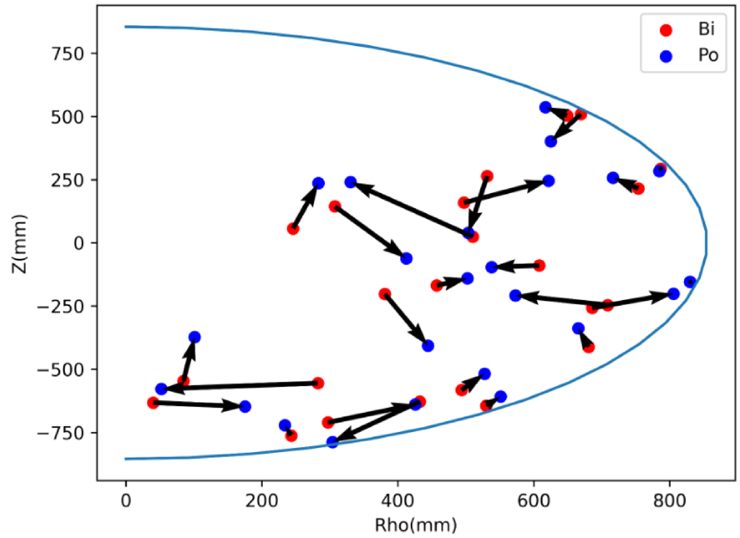

Figure 4.10: The positions of 24 dust ^{214}Bi and ^{214}Po particles, indicated with directional arrows, show an approximately uniform distribution within the detector.

dataset of operating the DEAP-3600 detector. Figure 4.11 illustrates the average number of dust events per day during the three-year runtime. Given that the rate of dust ^{214}Bi to ^{214}Po events is one dust event every 17.28 days. we might not observe any dust samples in the 2020 dataset, which only spans 13.06 days.

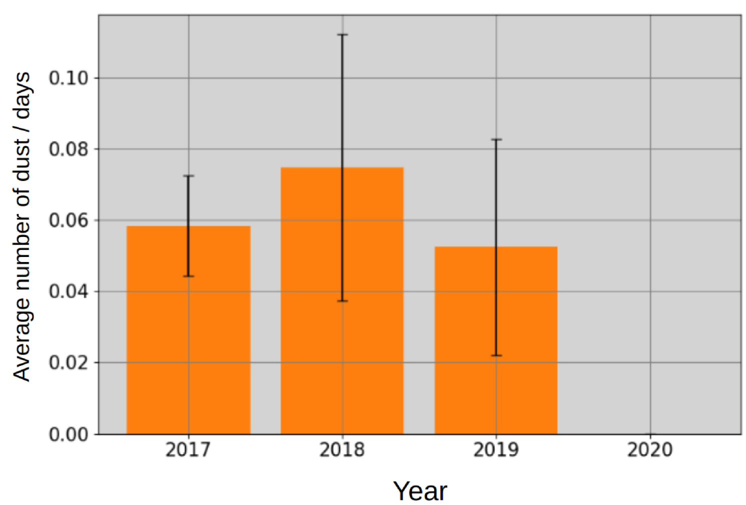

Figure 4.11: Graph shows average daily dust events vs year. With a dust ^{214}Bi to ^{214}Po rate of 1 event every 17.28 days, no dust samples expected in the 2020 dataset spanning only 13.06 days

The assumption regarding ^{214}Bi and ^{214}Po dust is that the half-life should exactly match those of ^{214}Bi and ^{214}Po. The energy of Bi is unaffected, while the energy of Po is degraded. Considering this fact and all of the aforementioned properties, such as position and time occurrence, we can conclude that these 24 events represent the first proof from a data aspect, demonstrating that dust can mimic a WIMP in data.

4.6.1 Comparing Fprompt of Dust and Surface ^{214}Bi-^{214}Po

Dark matter interacts with liquid argon, emitting high Fprompt signals with low energy, typically around 100-130 PE, reaching maximum energy at 200 PE. Surface alphas, on the other hand, possess lower energy due to their loss of energy in acrylic and TPB. Unlike other particles, they reconstruct on the surface and exhibit slightly lower Fprompt compared to dust events.

Dust events scattered throughout the central volume of the detector, sharing the high Fprompt characteristic with WIMPs. Consequently, distinguishing between dust events and WIMP events proves challenging. TPB-coated dust exhibits lower Fprompt within the ROI. Estimating the quantity of dust involves analyzing high-energy data and extrapolating it to lower energies through fitting. However, when dust is coated with TPB, this extrapolation varies, impacting the accuracy of the estimation process.

In this section, we will compare the Fprompt of dust and surface ^{214}Bi-^{214}Po. To gain an understanding of the nature of these 24 dust events and how they compare to the dust with coated TPB. In Figure 4.12, the Fprompt distribution of the dust and surface ^{214}Bi-^{214}Po is shown. The Fprompt distribution of the dust in Figure 4.12a has a higher mean and is narrower compared to the surface ^{214}Bi-^{214}Po in Figure 4.12b. We know that the surface ^{214}Bi-^{214}Po is affected by TPB, and the fact that these two distributions are different based on the mean and root mean square suggests that most of the 24 dust events are not TPB-coated.

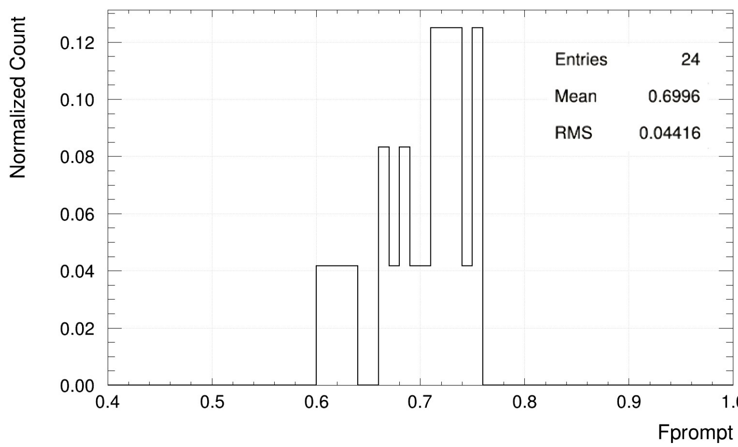

(a) Fprompt distribution of the dust events.

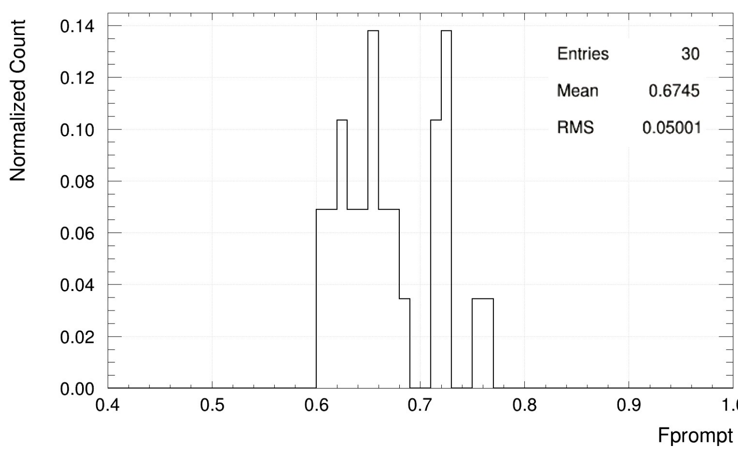

(b) Fprompt distribution of the surface events.

Figure 4.12: Fprompt distribution of dust and surface ^{214}Bi-^{214}Po. In these figures, normalized counts are used, where the number of events in each bin is divided by the total number of events.

Another method to compare two Fprompt distributions quantitatively is using a Monte Carlo permutation statistical test on their skewness. This method was first suggested by Fred Schuckman, a member of the DEAP collaboration. In this method, we use the skewness defined as follows:

$$\text{Skewness } = \frac{1}{n}\sum_{i=1}^{n}\left(\frac{X_i - \bar{X}}{\sigma}\right)^3, \tag{4.5}$$

where X_i are the data points, $\bar{X}$ is the mean, σ is the standard deviation, and n is the number of data points.

A step-by-step explanation of this method is provided below:

- Calculate the skewness of the Fprompt distributions for both dust and surface.
- Calculate the difference between the skewness values.
- Combine all the Fprompt values for dust and surface into a single array.
- Randomly shuffle the array and consider the first 24 values as dust and the remaining as surface.
- Calculate the difference in skewness between these two new arrays.
- Repeat these steps 10^6 times and plot the histogram of the final results.

The final result of the method described above is shown in Figure 4.13 alongside the difference in skewness between the dust and surface Fprompt distributions and a Gaussian fit to the distribution of randomly generated skewness values. The distance between the mean of the Gaussian fit and the skewness is 2.44σ , indicating a difference between the dust Fprompt distribution and the surface, suggesting that most of the dust events should not be coated with TPB.

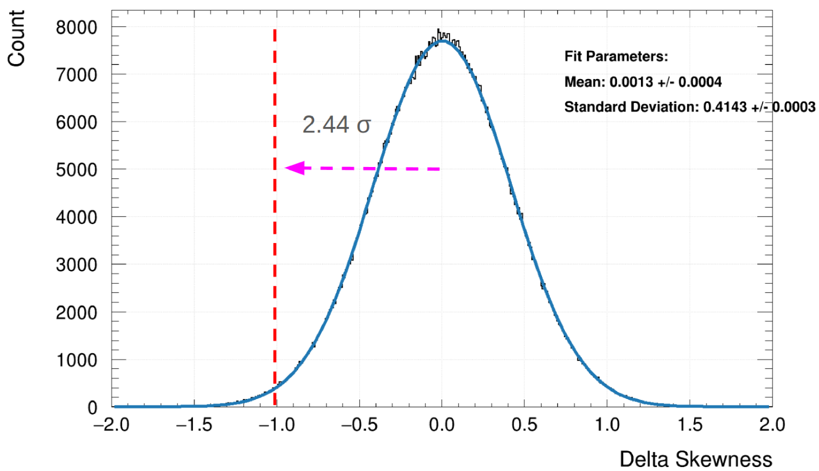

Figure 4.13: Quantitative comparison of dust and surface Fprompt distributions using Monte Carlo permutation statistical test on skewness. The results reveal a significant difference between the distributions, suggesting that most dust events are not coated with TPB.

Chapter 5

Alphas from ^{220}Rn ^{216}Po

5.1 Dataset and Cuts

The method employed and the clean results obtained in identifying ^{214}Bi-^{214}Po in Chapter 3 demonstrate that we can utilize the same approach to identify any other radioactive source in the detector with a short lifetime. Hence, by examining Figure 3.3 and Figure 3.4, it becomes evident that ^{220}Rn-^{216}Po presents itself as a good candidate for employing this method, given its relatively short half-life of 140 ms.

We seek α-α coincidences, defining events where $0.6 < F_{\mathrm{prompt}} < 0.8$, as illustrated in Figure 4.1. The flowchart for identifying ^{220}Rn-^{216}Po is presented in Figure 5.1. We implement an additional data-cleaning step to remove high-rate alpha events, the details of which are provided in the next section. The time window for detecting α-α coincidences is determined by the half-life of ^{220}Rn-^{216}Po that is 145 ms, resulting in a search window of 1.65 ms to 1.45 s. However, this extended time window yields numerous random events. Therefore, a distance cut of 200 mm is applied, which is shorter compared to the distance cut used for ^{214}Bi-^{214}Po.

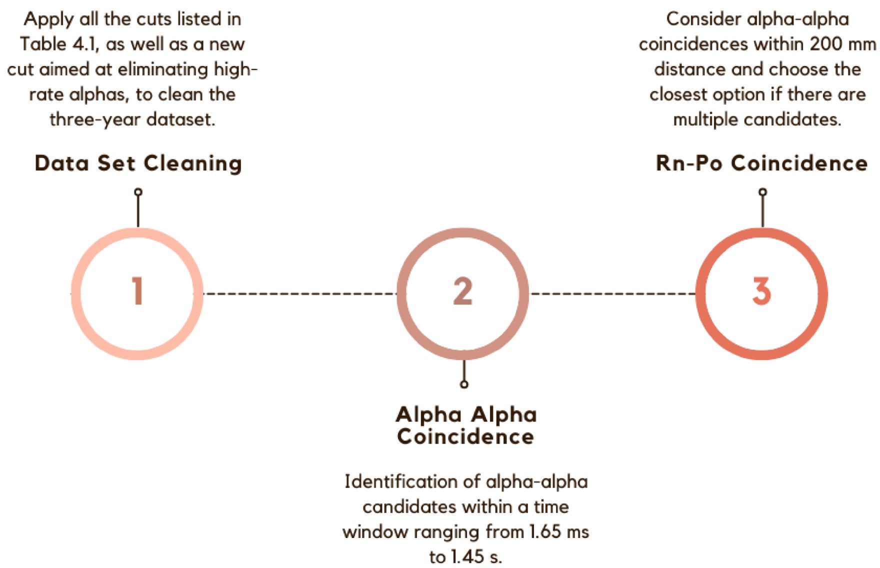

Figure 5.1: Flowchart illustrating the process for identifying ^{220}Rn-^{216}Po events, highlighting the sequential steps involved in the analysis.

5.1.1 High-Rate Alpha Events Cut

One of the main challenges we faced in the ^{220}Rn-^{216}Po study was the presence of numerous random low-energy events, which prevented us from obtaining a clean dataset with well-correlated decay times. We developed a new cut to remove these random events. We will discuss the properties of these random events and the cut we applied to filter them out. After applying all the cuts listed in Table 4.1, except the final one ($MBL_Z < 550$ mm), we retained 124,453 events in both gas and liquid argon. In Figure 5.2, the rate of alpha events is shown in both gas (Figure 5.2a) and liquid argon (Figure 5.2b). These figures indicate that the number of high-rate alpha events is greater in the gas region ($MBL_Z \geq 550$ mm) compared to liquid argon. After applying MBL_z, 105,227 events remain. However, even with this cut, some cases still exhibit high rates, as shown in Figure 5.2b.

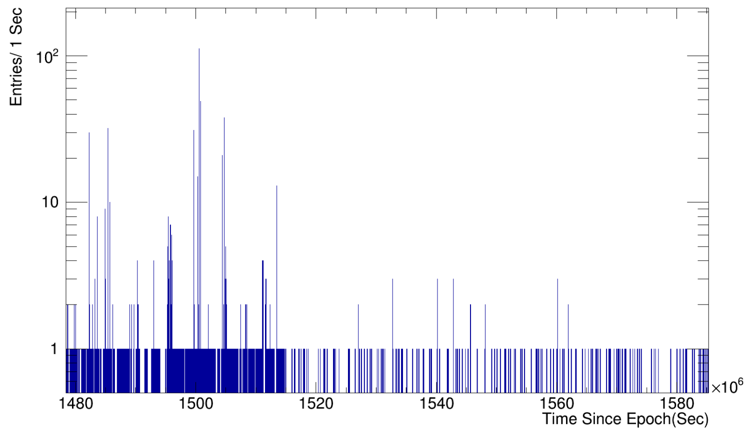

(a) Rate of alpha events in the gas argon ($MBL_Z \geq 550$ mm) per second. The x-axis represents the time since the epoch in seconds. Multiple high-rate alpha events appear abnormal in this figure.

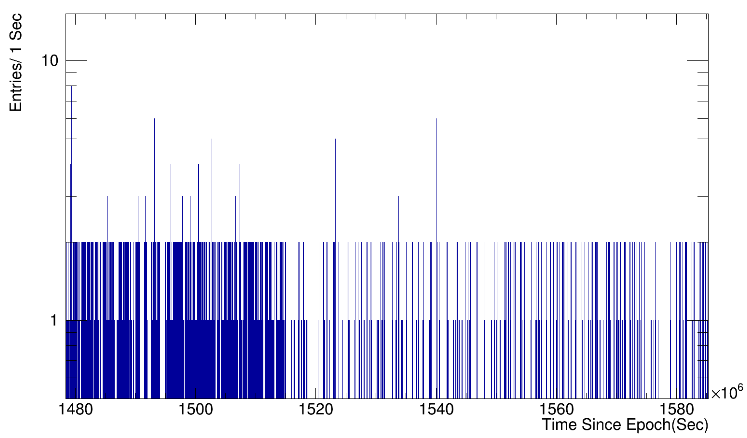

(b) Rate of alpha events in liquid argon ($MBL_Z < 550$ mm) per second. The x-axis represents the time since the epoch in seconds.

Figure 5.2: Rate of alpha events in liquid and gas argon per second.

The main focus of this study is on alphas that occur in liquid argon. To find the best cut, we need to create a distribution based on Figure 5.2b. First, we rebin this histogram to 10 minutes and make the distribution of the number of 10-minute intervals that is shown in Figure 5.3.

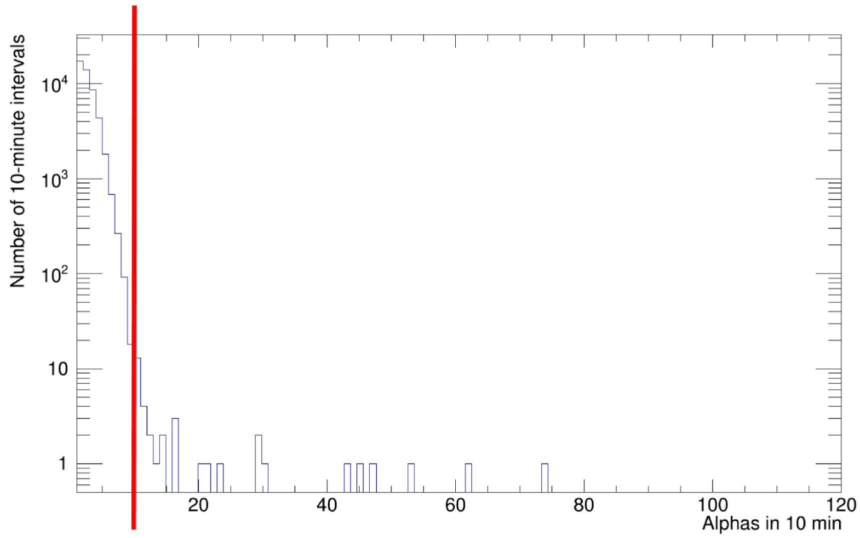

Figure 5.3: Distribution of the number of 10-minute intervals. The red line shows the cut used to filter high-rate alphas.

The rate cut is to remove any 10-minute rolling time window that includes more than 10 alphas. In Figure 5.4, we can see the Fprompt distribution of those alphas that pass and fail this cut. The second peak in Fprompt indicates that most of these high-rate alphas also have a high Fprompt.

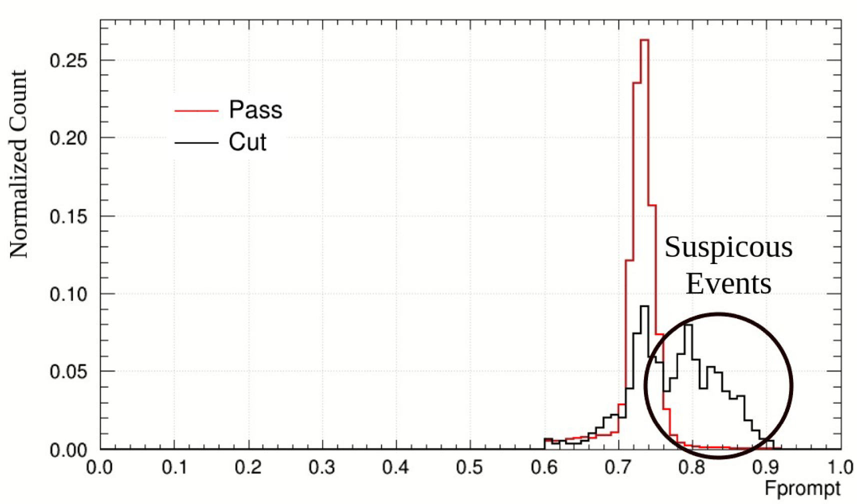

Figure 5.4: Histogram of Fprompt for alphas that fail or pass the rate cut. The black line represents failed alphas, while the red line represents passed alphas. Most of the failed alphas have a higher Fprompt.

Using this cut will remove 591 alpha events and 200 minutes of lifetime in our 414.76-day dataset. Most of the alphas have low energy. Figure 5.5 shows the positions of the high rate events from Figure 5.4 in the detector. We can see that these high-rate alphas occur in just three regions near the acrylic of the detector.

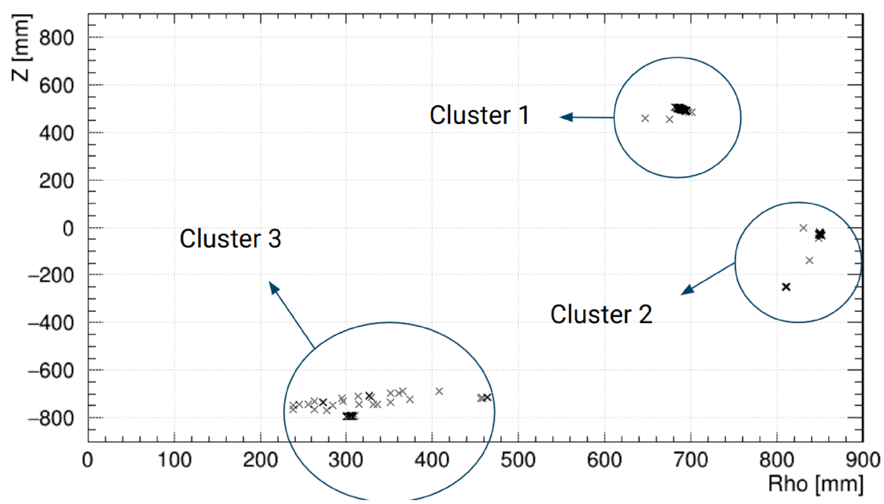

Figure 5.5: Positions of high-rate events: This figure shows that all of these events occur in just three regions within the detector. The source of these events in these three regions, despite the absence of any known source, remains unclear.

After applying all cuts in Table 4.1, including the high-rate alphas cut, 104,636 events remain for finding any ^{220}Rn ^{216}Po.

5.2 ^{220}Rn-^{216}Po

After applying all cuts and conditions in Figure 5.1 we can get 897 alpha-alpha events. in Figure 5.6 below the time difference between these alpha-alpha events is shown.

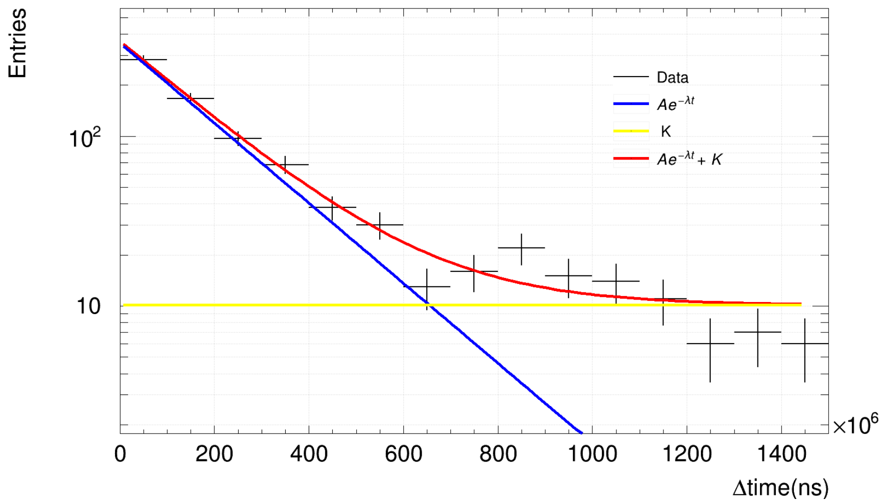

Figure 5.6: The time intervals between ^{220}Rn and ^{216}Po events. The yellow line depicts the fitting curve for accidental coincidences, whereas the blue line illustrates the exponential fit for ^{220}Rn and ^{214}Po events.

We expect the distribution of times to be given by the following equation:

$$P(t) = N_{\alpha-\alpha} \lambda t_{bin} e^{-\lambda t} + Const. \tag{5.1}$$

where:

- $N_{\text{RnPo}} = (66 \pm 6) \times 10$
- $\lambda = (5.4 \pm 0.4)(1/ns)$
- $Const. = 10 \pm 2$

Using the λ that we get from Equation 5.1, we can determine the half-life associated with the decay. This half-life ($t_{1/2} = 0.128 \pm 0.009$) s is within 2 σ of the 145 ms half-life of ^{220}Rn-^{216}Po decay chain, so most of these 897 events originate from the same chain. Comparing this result with the ^{214}Bi-^{214}Po decay chain shows that we observe more random events here. In Figure 5.7, we can see the 2D plot of the energy of the first alpha versus the second alpha. Generally, we expect to see full-energy alphas and a uniform range of degraded alphas. Therefore, the second region in the figure, which shows a high number of alpha events, requires further investigation.

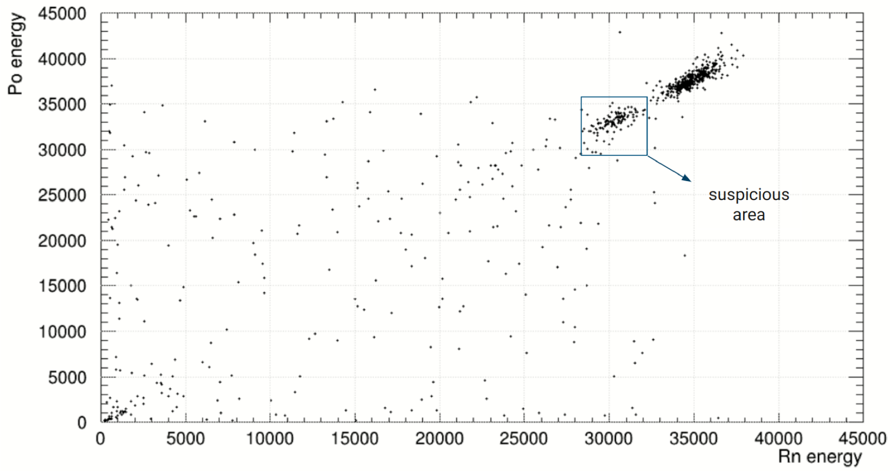

Figure 5.7: 2D plot of ^{216}Po energy versus ^{220}Rn energy. The marked area in this figure requires further investigation.

In Figure 5.8, the time difference for ^{220}Rn and ^{216}Po in the marked area of Figure 5.7 is shown. This figure indicates that most of the alpha events in this area are random.

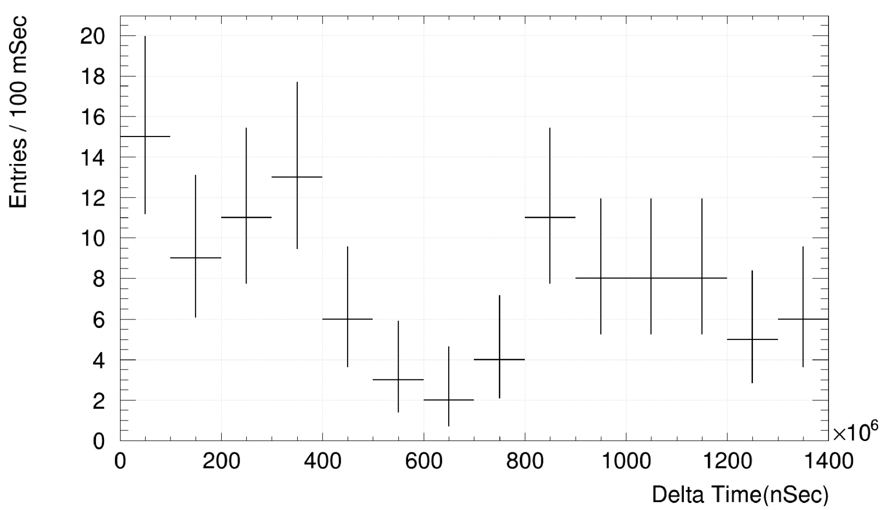

Figure 5.8: Time difference for events shown in Figure 5.7. This time difference indicates that most of these events are random.

The final time difference after removing all 113 random events is shown in Figure 5.9.

The total number of final ^{220}Rn-^{216}Po events is 679.

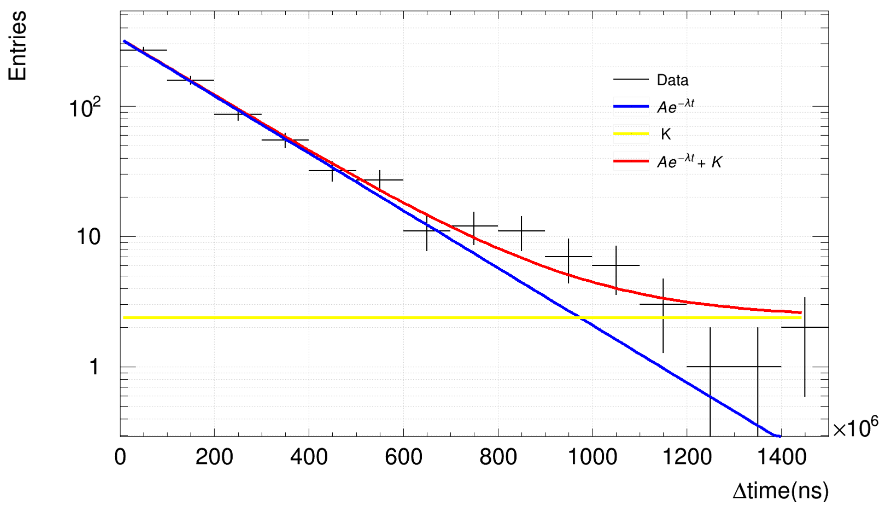

Figure 5.9: The final time intervals between ^{220}Rn and ^{216}Po events.

By applying the same approach of fitting like equation 5.1 we can find:

- $N_{\mathrm{RnPo}} = (65 \pm 6) \times 10$
- $\lambda = (5.0 \pm 0.3)(1/ns)$
- $Const. = 2 \pm 1$

By using the λ from the above fitting equation, we can calculate the half-life as $t_{1/2} = 0.137 \pm 0.009$ s, which is in close agreement with the known half-life of 0.145 s for the ^{220}Rn-^{216}Po decay chain. Another aspect to examine is the energy of ^{220}Rn-^{216}Po events. In Figure 5.10, the energy distribution is shown alongside a 2D plot of Fprompt versus the energy of these events. The energies of Rn and Po, shown in Figure 5.10d and Figure 5.10c, with peaks at 35,000 and 38,000 qPE, respectively, are in agreement with the full energy decay chain of ^{220}Rn-^{216}Po that are 6.4 and 6.9 Mev.

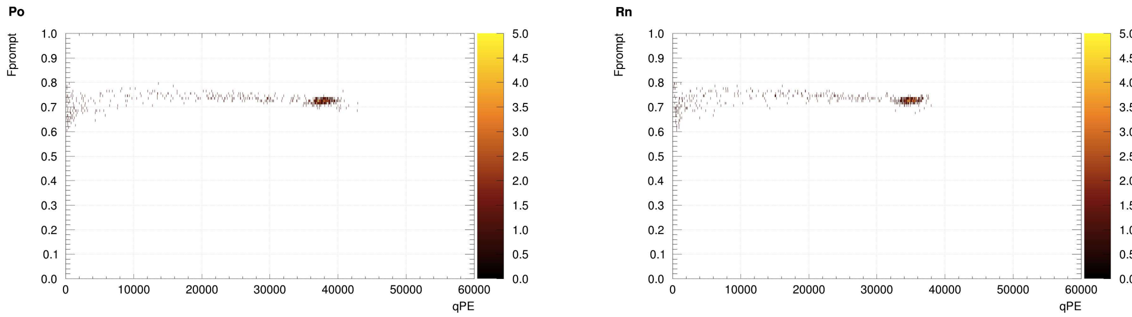

(a) Po Fprompt vs qPE. The colour bar represents the number of events.

(b) Rn Fprompt vs qPE. The colour bar represents the number of events.

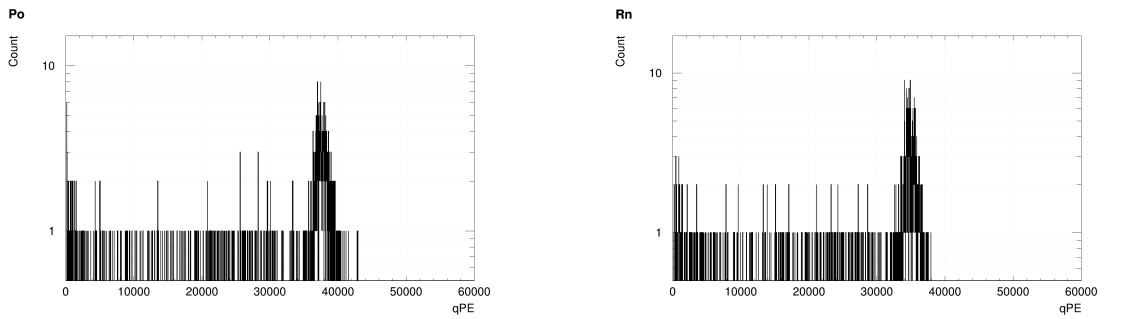

(c) Energy distribution of Po events.

(d) Energy distribution of Rn events.

Figure 5.10: The Fprompt vs. qPE and energy distribution of ^{220}Rn and ^{216}Po. The energy peaks in these figures are in agreement with the decay chain energies of ^{220}Rn and ^{216}Po.

Another expected characteristic of the decay chain is the uniform distribution of ^{220}Rn and ^{216}Po within the detector. Figure Figure 5.11 illustrates this approximate uniform distribution.

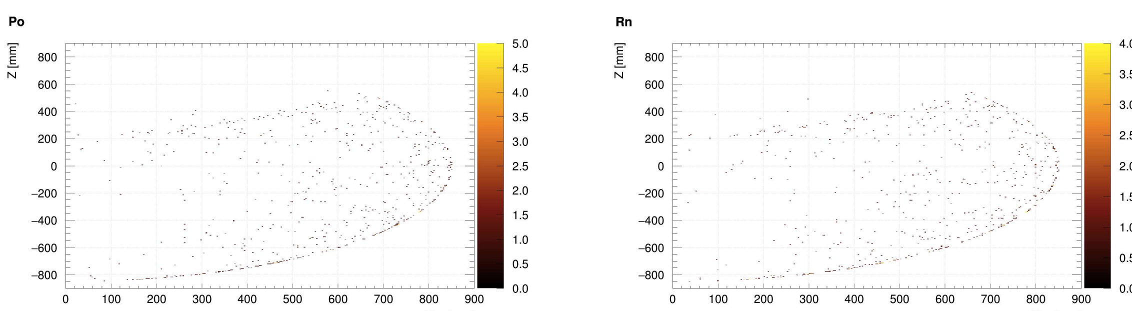

(a) Position of Po within detector. The colour bar represents the number of events.

(b) Position of Rn within detector. The colour bar represents the number of events.

Figure 5.11: The positions ^{220}Rn and ^{216}Po particles, show an approximately uniform distribution within the detector. The colour bar represents the number of events.

5.3 Low Energy Degraded ^{220}Rn-^{216}Po

5.3.1 Neck Alpha Cut

One of the main challenging background sources of alphas is those that occur within the acrylic neck flowguide surface. One of the ongoing studies in our group, led by Courtney Mielnichuk, is to compare the performance of our two position fitters, TF2 and MBL, for alphas that occur inside the acrylic neck. In this study, multiple ^{210}Po alphas are produced in the inner flowguide acrylic neck (Figure 5.12a). Figure 5.12b shows most of alphas have low energy and high Fprompt. In Figure 5.13 we compare the calculated TF2 with MBL. This comparison shows that one of the key differences for alphas in the acrylic neck is the difference between the z component of their TF2 and MBL positions. We will use this difference to define a cut and explore the low-degraded alphas from ^{220}Rn-^{216}Po to identify any neck events.

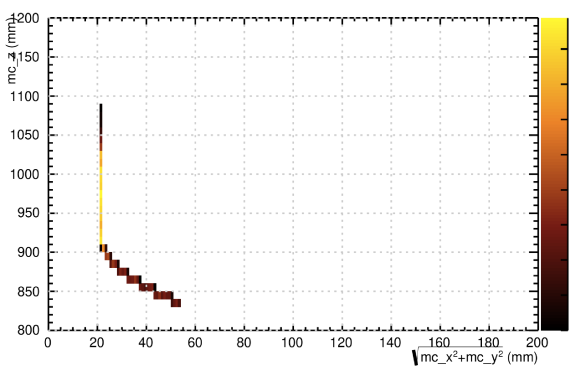

(a) True positions. The colour bar represents the number of events. mc_x and mc_y represent the Monte Carlo truth position in the x and y directions.

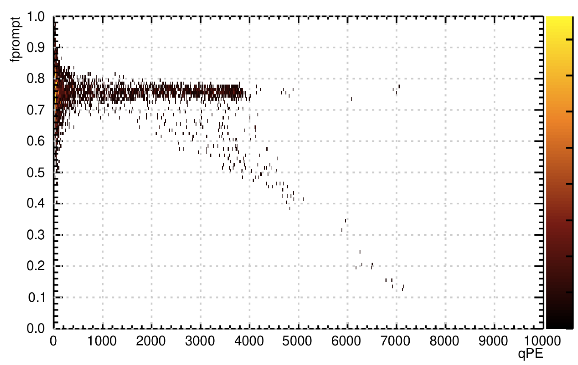

(b) Fprompt vs qPE. The colour bar represents the number of events.

Figure 5.12: True position and Fprompt vs qPE of Monte Carlo simulation alphas in the acrylic neck. Image courtesy of Courtney Mielnichuk.

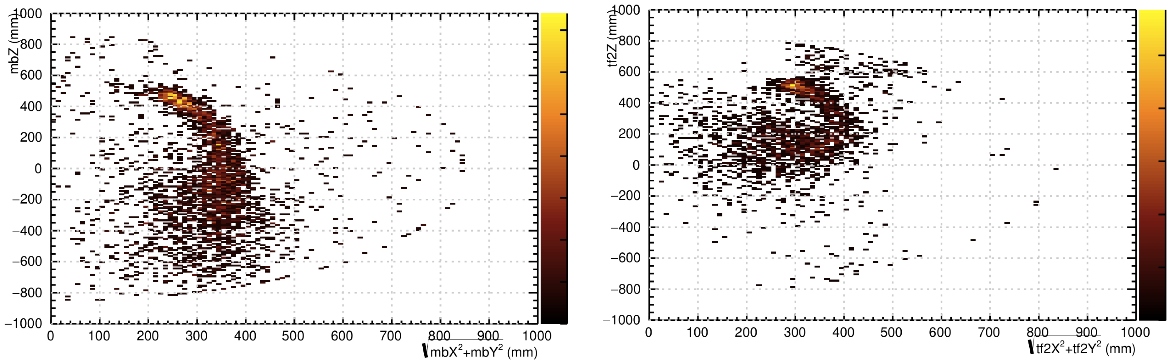

(a) MBLz vs MBLRho. The colour bar represents the number of events. mb_x and mb_y represent the MBL position in the x and y directions.

(b) TF2z vs TF2Rho. The colour bar represents the number of events. tf2_x and tf2_y represent the TF2 position in the x and y directions.

Figure 5.13: Positions of alphas based on the MBL and TF2 fitters in the detector. This result shows a key difference in the z component between these two fitters for neck alphas. Image courtesy of Courtney Mielnichuk.

In Figure 5.14, we can see the 3D positions of low-energy degraded alphas (qPE $<$ 10,000) from the ^{220}Rn-^{216}Po study, categorized into two groups: surface events (both MBLR $>$ 845) and events within the detector (both MBLR $\leq$ 845). Out of 49 alpha events detected near the surface, 3 have a significant difference between the z component of their TF2 and MBL positions, and these are tagged as neck events. Within the detector, 6 out of 10 events also show a significant difference in the z component between TF2 and MBL and are similarly tagged as neck events. One significant result is the consistency of this tagging criterion between ^{220}Rn and ^{216}Po alphas. If a ^{220}Rn event is tagged as a neck event, the related ^{216}Po will be tagged as well, indicating that both occurred in the neck region as expected.

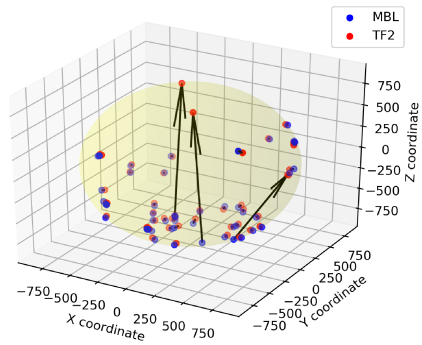

(a) Surface ^{220}Rn.

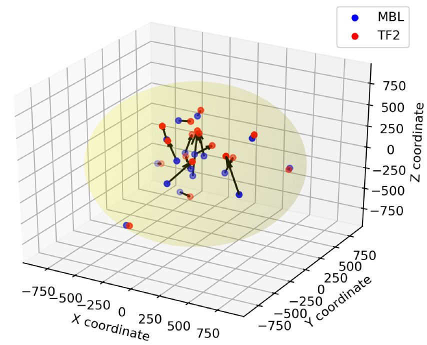

(b) ^{220}Rn within the detector.

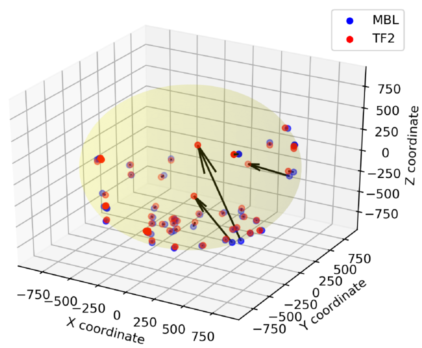

(c) Surface ^{216}Po.

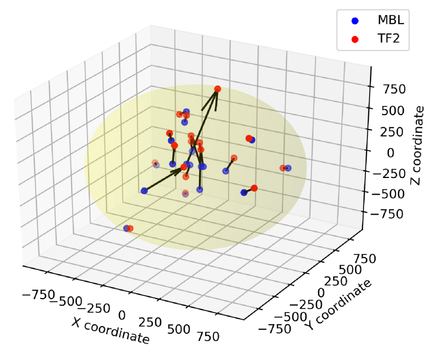

(d) ^{216}Po within the detector..

Figure 5.14: 3D position of ^{220}Rn and ^{216}Po. The blue dot is the coordinate of the alpha base on MBL, and the red dot is the coordinate based on TF2. An arrow between this blue and red dot shows the difference between these two fitters for the same event.

5.3.2 Comparing Fprompt

After applying all cuts, 92 alpha events on the surface and 20 alphas within the detector remain. We can compare the distribution of these alphas with the dust and surface alphas from ^{214}Bi-^{214}Po, as discussed in Section 4.6.1. In Figure 5.15, the Fprompt distributions for these two categories are shown.

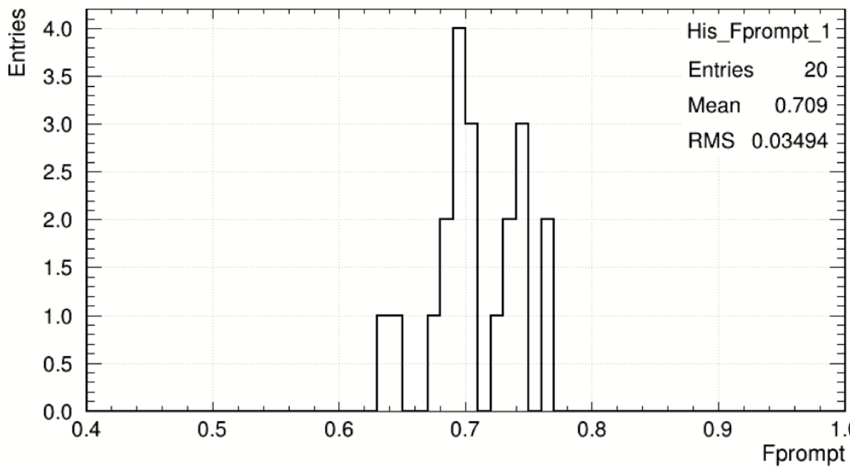

(a) Fprompt distribution of the 20 alphas (^{220}Rn and ^{216}Po) within the detector.

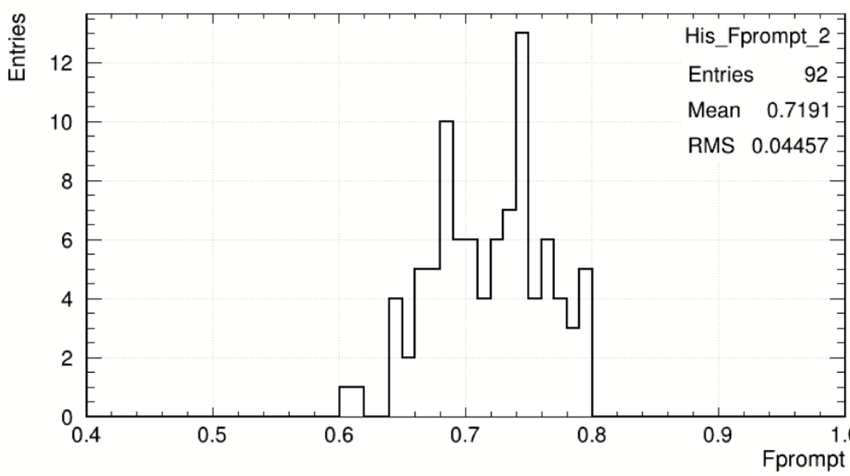

(b) Fprompt distribution of the 92 surface alphas (^{220}Rn and ^{216}Po).

Figure 5.15: Fprompt distribution of low degraded alpha events within and on surface of the detector from ^{220}Rn-^{216}Po.

Although the Fprompt distribution for alpha events on the surface has a wider range compared to dust, the mean Fprompt value is significantly higher. This result differs from what we expect and observe in the Fprompt distributions for dust and surface ^{214}Bi-^{214}Po, as shown in Figure 4.12.

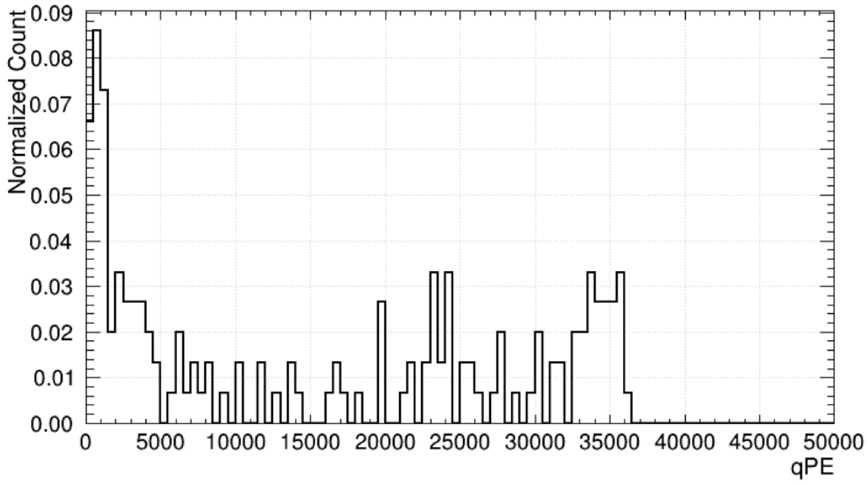

(a) Surface ^{220}Rn qPE energy distribution.

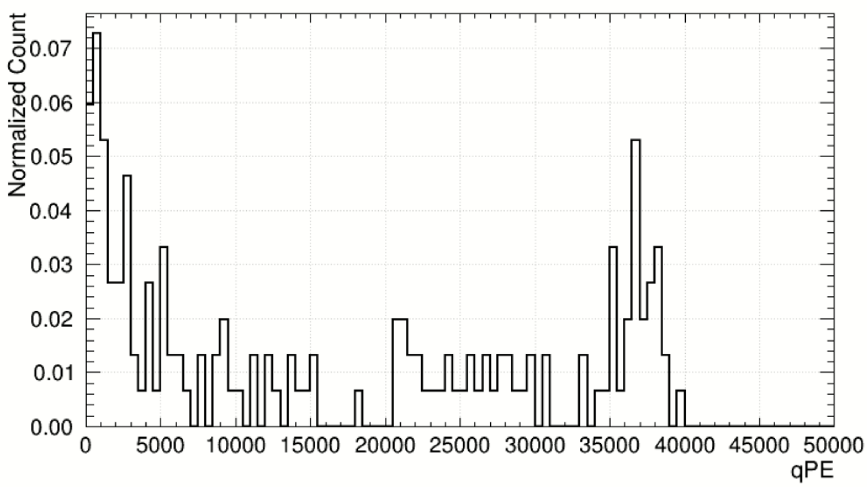

(b) Surface ^{216}Po qPE energy distribution.

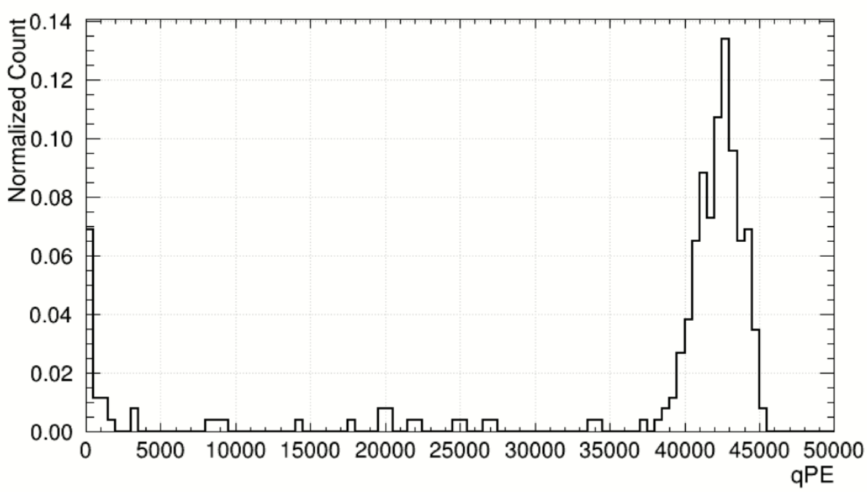

(c) Surface ^{214}Po qPE energy distribution.

Figure 5.16: Fprompt distribution of low degraded alpha events within and on surface of the detector from ^{220}Rn-^{216}Po.

To better understand the key differences between surface ^{214}Bi-^{214}Po and surface ^{220}Rn-^{216}Po, we should investigate the energy distribution of surface alphas in these two cases. In Figure 5.16, the energy distribution for alphas on the surface is shown without any energy cuts. The energy distribution of ^{214}Po in Figure 5.16c indicates that most of these alphas occur at full energy. In contrast, alphas from ^{220}Rn and ^{216}Po (Figure 5.16a and Figure 5.16b) exhibit a completely different pattern, with a high number of degraded alphas ranging from 200 qPE to full energy. This difference suggests a fundamental distinction between surface alphas in these two studies.

5.4 Toy Monte Carlo Simulation

One possible reason for the difference in alpha particles observed from the ^{214}Bi-^{214}Po and ^{220}Rn-^{216}Po chains is that the ^{220}Rn are produced uniformly throughout the acrylic material. Because ^{220}Rn is deep within the acrylic, alphas lose energy and leave the acrylic.

The alpha particle is a doubly-ionized helium atom, made up of 2 protons and two neutrons. An alpha particle has a mass of 4 atomic mass units (amu), which is approximately 8000 times the mass of an electron. As it travels through matter, the alpha particle primarily loses energy through ionization and excitation of atoms in the target material. Due to its large mass compared to atomic electrons, it can travel through matter in an almost straight line. This straight-line path simplifies the simulation of alphas in acrylic.

The small amount of energy lost by a particle as it travels a short distance is known as the differential energy loss, represented by $\frac{dE}{dx}$. This quantity, also referred to as the stopping power, measures how much energy an alpha particle loses per unit distance in a given material. The Bethe formula (equation 5.3) describes the stopping power in ergs per centimeter for a material made up of a single pure element [52].

$$-\frac{dE}{dx} = \frac{4\pi e^4 Z^2}{m_0 v^2} NB, \tag{5.2}$$

where

$$B = Z\left[\ln\left(\frac{2m_0v^2}{I_{\text{av}}}\right) - \ln\left(1 - \frac{v^2}{c^2}\right) - \frac{v^2}{c^2}\right], \tag{5.3}$$

where

- Z = the atomic number of the particle.
- e = electronic charge.
- m_0 = rest mass of an electron.
- v = the velocity of the charged particle (cm/s).
- N = the number of atoms per cm^3 in the target material.
- I_{av} = mean ionization potential of the target.
- E = energy of the particle.

The velocity for alpha particles with an energy of less than 10 MeV is less than 2.3% of the speed of light. As a result, the v^2/c^2 terms in equation (5.4) can be considered negligible and thus ignored. Equation (5.3) illustrates how the stopping power relies on the charge and velocity of the charged particle, as well as the atomic density and charge per atom in the target material.

In this toy Monte Carlo simulation, we used the dataset for alphas in acrylic from the NIST ASTAR database. This dataset consists of three columns: the kinetic energy of alpha (MeV), total stopping power (MeV $\times$ cm^2/g), and projected range (g/cm^2) [53]. Figure 5.17 shows the relationship between alpha energy and projected range, along with the linear interpolation of this data.

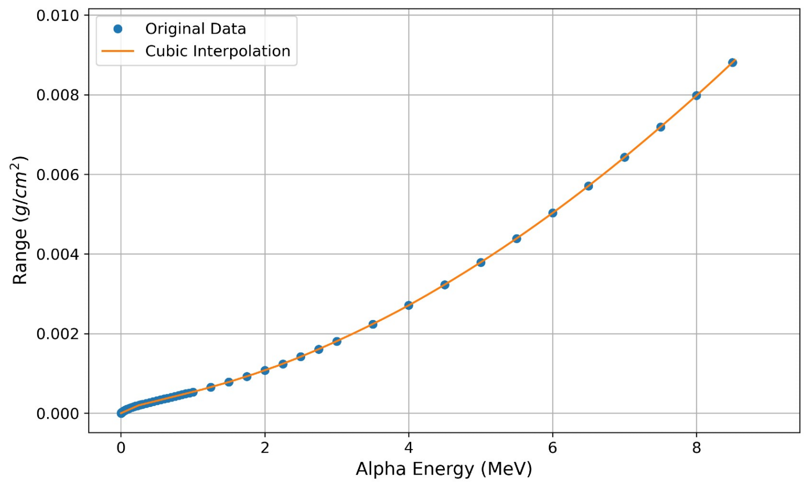

Figure 5.17: Range vs. energy. The blue points represent the dataset, and the orange line shows the linear interpolation.

In the diagram Figure 5.18, the structure of the particle inside the acrylic is depicted. The simulation process goes as follows:

- Alpha particles are randomly generated at various depths within the acrylic medium. The distribution of these initial depths is uniform, ranging between 0 and 60 microns, ensuring that the particles are equally likely to originate from any point within the acrylic.
- Each alpha particle is assigned a random direction with a uniform distribution of $cos\theta$ between 0 and 1 upon generation. This randomness simulates the various possible trajectories the particles could take as they travel through the acrylic.
- For each alpha particle, the distance (d) to the surface of the acrylic is calculated based on its initial position and direction.
- The density of acrylic in DEAP-3600 is 1.18 g/cm^3. By using this density, we can calculate the energy loss versus distance from the NIST dataset as follows:

$$Distance(cm) = \frac{Range(g/cm^2)}{Density(g/cm^3)}. \tag{5.4}$$

- Using this relation and accounting for the alphas to start with full energy (for ^{220}Rn with 6.4 MeV and ^{216}Po with 6.9 MeV), we can calculate the energy loss and final energy that alphas have when they exit the acrylic, if it is possible.

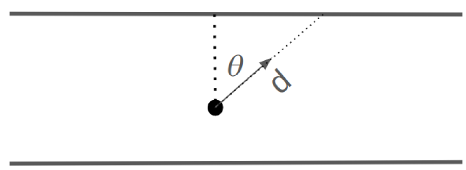

Figure 5.18: Diagram of an alpha particle inside an acrylic material, showing a random direction and position.

The 2D Figure 5.19 depicts the energy of ^{216}Po versus ^{220}Rn. It shows two clusters of alphas: cluster 1 includes 26 events with both full energy ^{220}Rn and ^{216}Po, while the other cluster consists of 125 events with low degraded energy alphas. This graph suggests that there are two populations of alphas: the first group consists of alphas near the surface of the acrylic, and the second group comprises alphas deep within the acrylic. This 2D plot shows that if the first alpha is degraded, the second alpha is degraded as well.

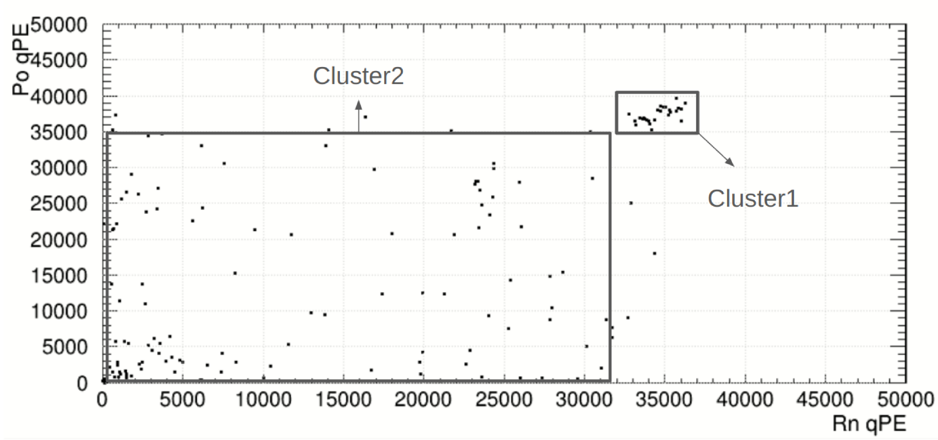

Figure 5.19: ^{216}Po vs ^{220}Rn. There are two clusters of alphas in this graph: full energy and low degraded.

In the simulation, we begin with alpha particles having an energy of 6.9 MeV. We generate alphas in the range of 0 to 4 microns, representing cluster 1, and alphas in the deep acrylic layer of 4 to 60 microns, representing cluster 2, with a ratio of 1 to 4.8 between the full energy and degraded alpha. Figure 5.20 shows the energy distribution for these generated alpha particles.

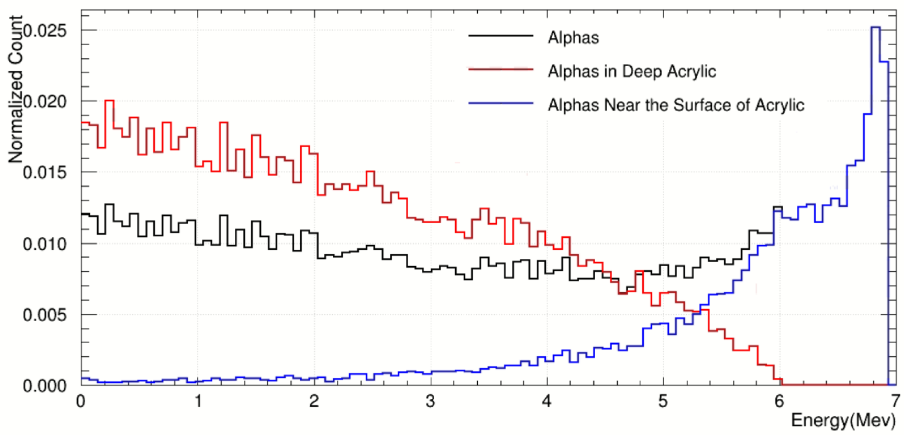

Figure 5.20: The energy distribution of alphas in acrylic. The red line represents alphas at a depth of 4 to 60 microns in acrylic, and the blue line represents alphas within 0 to 4 microns. The black line shows the total distribution.

In Figure 5.21, a comparison is presented between the results of the Monte Carlo simulation and the energy distribution of ^{216}Po from the ^{220}Rn-^{216}Po decay chain. This basic Monte Carlo simulation illustrates the wide range of alpha particle energies (ranging from 2000-34000 qPE) observed in the ^{220}Rn-^{216}Po chain (Figure 5.16b), a phenomenon that is not observed in alpha particles from the ^{214}Bi-^{214}Po chain (Figure 5.16c). Additionally, the simulation can account for the peak corresponding to the full energy of the alphas, but it is unable to explain the peak up to 2000 qPE, requiring further investigation.

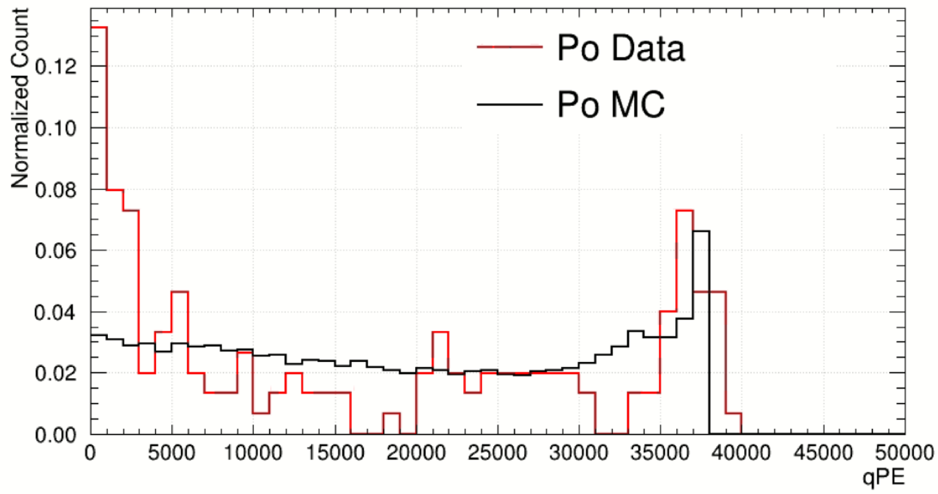

Figure 5.21: Comparison between the Monte Carlo simulation and the energy distribution of ^{216}Po.

Chapter 6

Conclusions

DEAP-3600 has implemented several strategies to minimize background events in its dark matter search. Despite efforts like underground placement, material selection, and advanced discrimination techniques, challenges remain due to alpha decays from shadowed sources such as acrylic vessels neck and dust, as they can mimic dark matter signals.

In this thesis, we successfully identified the ^{214}Bi-^{214}Po decay chain in the three-year dataset from DEAP-3600 by applying various low-level and pile-up cuts to clean the data. We used time and distance criteria to confidently identify ^{214}Bi-^{214}Po events. The half-life of ^{214}Po, as calculated in this study, aligns with the expected value. Experimental results in DEAP showed evidence of dust in the liquid argon, which led to extensive efforts by the DEAP collaboration to simulate dust in Monte Carlo in order to account for low degraded alphas attributed to dust. However, prior to our study, there was no proof of dust events in the DEAP-3600 data. The results of the ^{214}Bi-^{214}Po chain illustrate that low-degraded alphas can originate from the ^{214}Bi-^{214}Po chain within dust. The origin of the dust is crucial, especially whether it is TBP-coated or non-TBP-coated. A comparison of the dust dataset with surface alphas from the ^{214}Bi-^{214}Po chain, mainly influenced by TPB, revealed a 2.44σ difference in the distribution of Fprompt, suggesting that most dust events are not TPB-coated.

We have successfully identified ^{220}Rn-^{216}Po events using the method that was previously used for ^{214}Bi-^{214}Po. In the last chapter, we applied two additional cuts to filter out the high-rate alphas that occur in three specific regions of the detector near the surface, as well as to eliminate any neck alphas. This was done to minimize background. One interesting result is that the implementation of the neck events cut was successful, as alphas from Rn and Po both failed this specific cut, indicating that both Rn and Po originate from the acrylic vessels neck. We compared the distributions of these alphas with those from dust and surface involving ^{214}Bi-^{214}Po. Our data revealed that surface alpha events have a wide Fprompt distribution but a higher mean value compared to dust alphas, deviating from the expected pattern observed with ^{214}Bi-^{214}Po. To better understand the observed differences, we used a toy Monte Carlo simulation, which suggested that alpha particles from ^{220}Rn-^{216}Po lose energy due to Rn contamination of the acrylic. The simulation involved generating alpha particles within the acrylic and calculating their energy loss based on depth and direction. The simulation's findings partially aligned with the observed data, revealing a wide range of surface alpha energies in the ^{220}Rn-^{216}Po decay chain, a phenomenon not seen in the ^{214}Bi-^{214}Po chain. However, some discrepancies, such as unexplained peak around 200 qPE in the energy distribution, suggest the need for further investigation.

References

[1] P. D. Group *et al.*, "Review of particle physics," *Progress of Theoretical and Experimental Physics*, vol. 2020, no. 8, p. 083C01, 2020 (cit. on pp. 1, 6, 7).

[2] J. Billard *et al.*, "Direct detection of dark matter—appec committee report," *Reports on Progress in Physics*, vol. 85, no. 5, p. 056 201, 2022 (cit. on pp. 1, 11).

[3] J. Woithe and M. Kersting, "Bend it like dark matter!" *Physics Education*, vol. 56, no. 3, p. 035 011, 2021 (cit. on pp. 1, 4).

[4] H. Andernach and F. Zwicky, "English and spanish translation of zwicky's (1933) the redshift of extragalactic nebulae," *arxiv preprint arxiv:1711.01693*, 2017 (cit. on p. 2).

[5] F. Zwicky, "On the masses of nebulae and of clusters of nebulae," *The Astrophysical Journal*, vol. 86, p. 217, 1937 (cit. on p. 2).

[6] F. Zwicky, "On the large scale distribution of matter in the universe," *Physical Review*, vol. 61, no. 7-8, p. 489, 1942 (cit. on p. 2).

[7] K. C. Freeman, "On the disks of spiral and s0 galaxies," *Astrophysical Journal, vol. 160, p. 811*, vol. 160, p. 811, 1970 (cit. on p. 2).

[8] V. C. Rubin and W. K. Ford Jr, "Rotation of the andromeda nebula from a spectroscopic survey of emission regions," *The Astrophysical Journal*, vol. 159, p. 379, 1970 (cit. on p. 2).

[9] J. Beringer *et al.*, "Review of particle physics," *Physical Review D*, vol. 86, no. 1, 2012 (cit. on p. 2).

[10] T. S. Van Albada *et al.*, "Distribution of dark matter in the spiral galaxy ngc 3198," *The Astrophysical Journal*, vol. 295, pp. 305–313, 1985 (cit. on p. 2).

[11] Y Friedman and J. Steiner, "Gravitational deflection in relativistic Newtonian dynamics," *Europhysics Letters*, vol. 117, no. 5, p. 59 001, 2017 (cit. on p. 3).

[12] D. Clowe *et al.*, "A direct empirical proof of the existence of dark matter," *The Astrophysical Journal*, vol. 648, no. 2, p. L109, 2006 (cit. on pp. 3, 4).

[13] A. A. Penzias and R. W. Wilson, "A measurement of excess antenna temperature at 4080 mhz," pp. 873–876, 1979 (cit. on p. 4).

[14] G. Bertone, D. Hooper, and J. Silk, "Particle dark matter: Evidence, candidates and constraints," *Physics reports*, vol. 405, no. 5-6, pp. 279–390, 2005 (cit. on p. 5).

[15] N. Aghanim *et al.*, "Planck 2018 results-vi. cosmological parameters," *Astronomy & Astrophysics*, vol. 641, A6, 2020 (cit. on p. 5).

[16] J. L. Feng, "Dark matter candidates from particle physics and methods of detection," *Annual Review of Astronomy and Astrophysics*, vol. 48, pp. 495–545, 2010 (cit. on p. 6).

[17] G. Jungman, M. Kamionkowski, and K. Griest, "Supersymmetric dark matter," *Physics Reports*, vol. 267, no. 5-6, pp. 195–373, 1996 (cit. on p. 7).

[18] M. Drees, "Dark matter theory," *arxiv preprint arxiv:1811.06406*, 2018 (cit. on p. 7).

[19] M. Dine and W. Fischler, "The not-so-harmless axion," *Physics Letters B*, vol. 120, no. 1-3, pp. 137–141, 1983 (cit. on p. 8).

[20] B. J. Kavanagh and A. M. Green, "Improved determination of the wimp mass from direct detection data," *Physical Review D*, vol. 86, no. 6, p. 065 027, 2012 (cit. on p. 9).

[21] R Bernabei *et al.*, "First results from dama/libra and the combined results with dama/nai," *The European Physical Journal C*, vol. 56, pp. 333–355, 2008 (cit. on p. 9).

[22] M. Felcini, "Searches for dark matter particles at the LHC," *arXiv preprint arXiv:1809.06341*, 2018 (cit. on p. 9).

[23] P. J. Fox *et al.*, "Missing energy signatures of dark matter at the LHC," *Physical Review D*, vol. 85, no. 5, p. 056 011, 2012 (cit. on p. 9).

[24] K Abe *et al.*, "Indirect search for dark matter from the galactic center and halo with the super-kamiokande detector," *Physical Review D*, vol. 102, no. 7, p. 072 002, 2020 (cit. on p. 10).

[25] A Albert *et al.*, "Combined search for neutrinos from dark matter self-annihilation in the galactic center with Antares and Icecube," *Physical Review D*, vol. 102, no. 8, p. 082 002, 2020 (cit. on p. 10).

[26] M. Ackermann *et al.*, "The first fermi-lat gamma-ray burst catalog," *The Astrophysical Journal Supplement Series*, vol. 209, no. 1, p. 11, 2013 (cit. on p. 10).

[27] J. Aalbers *et al.*, "First dark matter search results from the lux-zeplin (lz) experiment," *Physical review letters*, vol. 131, no. 4, p. 041 002, 2023 (cit. on p. 12).

[28] R Agnese *et al.*, "Improved wimp-search reach of the CDMS ii germanium data," *Physical Review D*, vol. 92, no. 7, p. 072 003, 2015 (cit. on p. 11).

[29] P. Agnes *et al.*, "Darkside-50 532-day dark matter search with low-radioactivity argon," *Physical Review D*, vol. 98, no. 10, p. 102 006, 2018 (cit. on p. 11).

[30] D. Akerib *et al.*, "Results from a search for dark matter in the complete LUX exposure," *Physical review letters*, vol. 118, no. 2, p. 021 303, 2017 (cit. on p. 11).

[31] X. Collaboration *et al.*, "Dark matter search results from a one ton-year exposure of xenon1t," *Physical review letters*, vol. 121, no. 11, p. 111 302, 2018 (cit. on p. 11).

[32] X. Cui *et al.*, "Dark matter results from 54-ton-day exposure of Pandax-ii experiment," *Physical review letters*, vol. 119, no. 18, p. 181 302, 2017 (cit. on p. 11).

[33] P.-A. Amaudruz *et al.*, "Design and construction of the DEAP-3600 dark matter detector," *Astroparticle Physics*, vol. 108, pp. 1–23, 2019 (cit. on pp. 13, 15, 19, 20, 24, 35).

[34] R Ajaj *et al.*, "Search for dark matter with a 231-day exposure of liquid argon using deap-3600 at Snolab," *Physical Review D*, vol. 100, no. 2, p. 022 004, 2019 (cit. on pp. 13, 15–17, 27, 30, 34).

[35] A Hitachi, T Doke, and A Mozumder, "Luminescence quenching in liquid argon under charged-particle impact: Relative scintillation yield at different linear energy transfers," *Physical Review B*, vol. 46, no. 18, p. 11 463, 1992 (cit. on p. 13).

[36] T. Doke *et al.*, "Absolute scintillation yields in liquid argon and xenon for various particles," *Japanese journal of applied physics*, vol. 41, no. 3R, p. 1538, 2002 (cit. on pp. 13–15).

[37] V. Chepel and H. Araújo, "Liquid noble gas detectors for low energy particle physics," *Journal of Instrumentation*, vol. 8, no. 04, R04001, 2013 (cit. on p. 14).

[38] A. Kemp, "Using the profile likelihood method to search for dark matter using the deap-3600 detector," Ph.D. dissertation, Royal Holloway, University of London, 2020 (cit. on p. 15).

[39] P Adhikari *et al.*, "Pulse-shape discrimination against low-energy ar-39 beta decays in liquid argon with 4.5 tonne-years of deap-3600 data," *The European Physical Journal C*, vol. 81, pp. 1–13, 2021 (cit. on p. 15).

[40] F Duncan, A. Noble, and D Sinclair, "The construction and anticipated science of snolab," *Annual Review of Nuclear and Particle Science*, vol. 60, pp. 163–180, 2010 (cit. on pp. 17, 18).

[41] C. Jillings and D. Collaboration, "Control of contamination of radon-daughters in the deap-3600 acrylic vessel," in *AIP Conference Proceedings*, American Institute of Physics, vol. 1549, 2013, pp. 86–89 (cit. on pp. 18, 28).

[42] P.-A. Amaudruz *et al.*, "In-situ characterization of the hamamatsu r5912-hqe photomultiplier tubes used in the deap-3600 experiment," *Nuclear Instruments and Methods in Physics Research Section A: Accelerators, Spectrometers, Detectors and Associated Equipment*, vol. 922, pp. 373–384, 2019 (cit. on pp. 20, 21).

[43] V. Gehman *et al.*, "Fluorescence efficiency and visible re-emission spectrum of tetraphenyl butadiene films at extreme ultraviolet wavelengths," *Nuclear Instruments and Methods in Physics Research Section A: Accelerators, Spectrometers, Detectors and Associated Equipment*, vol. 654, no. 1, pp. 116–121, 2011 (cit. on p. 21).

[44] B. Broerman *et al.*, "Application of the tpb wavelength shifter to the deap-3600 spherical acrylic vessel inner surface," *Journal of Instrumentation*, vol. 12, no. 04, P04017, 2017 (cit. on p. 21).

[45] P.-A. Amaudruz *et al.*, "The data acquisition architecture for the dark matter experiment using argon pulse-shaped discrimination"—deap-3600," in *2016 IEEE-NPSS Real Time Conference (RT)*, IEEE, 2016, pp. 1–7 (cit. on p. 23).

[46] J. Calvo *et al.*, "Backgrounds and pulse shape discrimination in the ardm liquid argon tpc," *Journal of Cosmology and Astroparticle Physics*, vol. 2018, no. 12, p. 011, 2018 (cit. on p. 25).

[47] R Ajaj *et al.*, "Electromagnetic backgrounds and potassium-42 activity in the DEAP-3600 dark matter detector," *Physical Review D*, vol. 100, no. 7, p. 072 009, 2019 (cit. on p. 25).

[48] J. A. Formaggio and C. Martoff, "Backgrounds to sensitive experiments underground," *Annu. Rev. Nucl. Part. Sci.*, vol. 54, pp. 361–412, 2004 (cit. on p. 28).

[49] H. M. O'Keeffe, "Low energy background in the ncd phase of the sudbury neutrino observatory," Ph.D. dissertation, University of Oxford, 2008 (cit. on pp. 29, 30).

[50] A. Grobov and A. Ilyasov, "Boosted decision trees approach to neck alpha events discrimination in DEAP-3600 experiment," *Phys. Scripta*, vol. 95, no. 7, L. Bravina *et al.*, Eds., p. 074 007, 2020. DOI: 10.1088/1402-4896/ab8dff. arXiv: 2009.00895 [physics.ins-det] (cit. on p. 33).

[51] C. Mielnichuk, "A likelihood ratio algorithm forremoving localized alpha particle backgrounds in the deap-3600 detector," 2017. [Online]. Available: https://era.library.ualberta.ca/items/20cdb83a-3fcc-4f46-b707-736ecdc609e5 (cit. on p. 34).

[52] J. D. Cockcroft, "Experimental nuclear physics," *Nature*, vol. 175, pp. 53–54, 1955. [Online]. Available: https://api.semanticscholar.org/CorpusID:4249052 (cit. on p. 69).

[53] National Institute of Standards and Technology, *Astar: Stopping-power and range tables for electrons, protons, and helium ions*, 2014. [Online]. Available: https://physics.nist.gov/PhysRefData/Star/Text/ASTAR-t.html (cit. on p. 70).